

Syracuse University

**SURFACE**

---

Dissertations - ALL

SURFACE

---

August 2018

## Dispersive Transport and Drift Mobilities in Methylammonium Lead Iodide Perovskites

Brian Maynard  
*Syracuse University*

Follow this and additional works at: <https://surface.syr.edu/etd>



Part of the [Physical Sciences and Mathematics Commons](#)

---

### Recommended Citation

Maynard, Brian, "Dispersive Transport and Drift Mobilities in Methylammonium Lead Iodide Perovskites" (2018). *Dissertations - ALL*. 927.  
<https://surface.syr.edu/etd/927>

This Dissertation is brought to you for free and open access by the SURFACE at SURFACE. It has been accepted for inclusion in Dissertations - ALL by an authorized administrator of SURFACE. For more information, please contact [surface@syr.edu](mailto:surface@syr.edu).

## **Abstract**

Perovskite solar cells (PSCs) have impacted the photovoltaic industry over the past decade with unprecedented boosts in photo-conversion efficiencies. Perovskites' dramatic rise has been due to borrowed ideas and research from other types of solar cell geometries. The initial surge in perovskite research started in 2009 with the discovery of unusually long photocharge carrier lifetimes and ambipolar diffusion. These discoveries changed the geometry of the solar cell from a dye-sensitized structure to n-i-p. The work done in this dissertation focuses on thin film methylammonium lead iodide perovskites in n-i-p structures made by the National Renewable Energy Laboratory and Iowa State University. The initial goal of this research was to use photo carrier time-of-flight measurements to determine the drift mobilities of electrons and holes in the perovskite methylammonium lead iodide. I found evidence of dispersive transport for both photocharge carriers. I have made transient temperature-dependent studies of the drift mobility and the dispersion parameter, under otherwise normal device operating conditions. The low values of the electron and hole drift mobilities,  $\sim 10^{-1} \text{ cm}^2/\text{Vs}$ , under operating conditions suggest that the optimal thickness of the perovskite layer can be determined via calculation. The dispersive nature of perovskite thin films makes such calculations complicated. I propose, based on the temperature dependent studies of my work, that photocharge transport in perovskite thin films is spatially dispersive.

Dispersive Transport and Drift Mobilities in Methylammonium Lead Iodide Perovskites

by

Brian Maynard

B.A. Physics, State University of New York at Potsdam

B.A. Mathematics, State University of New York at Potsdam

Dissertation

Submitted in partial fulfillment of requirements for the degree of

Doctor of Philosophy in Physics

Syracuse University

August 2018

Copyright © Brian Maynard 2018

All Rights Reserve

## **ACKNOWLEDGEMENTS**

I would like to thank the Physics Department at Syracuse University for giving me the opportunity to earn my Ph.D. I have learned a great deal inside and outside of the courses offered and made some great friends along the way that certainly eased the strain of this degree. I would like to thank Patty Whitmore for all of her help and for introducing me to the Center for Learning and Student Success (CLASS) Office which gave me an opportunity to finish my degree in Syracuse. I would like to thank all of my friends at CLASS and particularly Samantha Johnston for being accommodating with my hours and training me to be a better instructor.

I would also like to thank Steluta Dinca, Hui Zhao, and Qi Long for their guidance on several projects. This work would not have been possible without funding from the National Science Foundation or samples from Vikram Dalal and Kai Zhu. Great thanks belong to my advisor Eric A. Schiff for being exceptionally patient and sharing some of his wisdom with me.

To my family and Marissa Bartz for effective motivation and belief in me. The end might not have happened if it wasn't for all of you.

## TABLE OF CONTENTS

<b>1. INTRODUCTION.....</b>	<b>1</b>
1.1. PEROVSKITES RISE TO THE SPOTLIGHT .....	3
1.2. DRIFT MOBILITY .....	6
1.3. NORMAL AND DISPERSIVE TRANSPORT .....	7
1.3.1. NORMAL TRANSPORT MODEL.....	8
1.3.2. DISPERSIVE TRANSPORT MODEL .....	9
1.4. TIME-OF-FLIGHT.....	11
1.5. THESIS RELEVANCE .....	14
<b>2. CHARACTERIZATION AND MEASUREMENTS OF PSC .....</b>	<b>17</b>
2.1 FABRICATION AND DEVICE CHARACTERIZATION.....	17
2.1.1 FABRICATION.....	17
2.1.1.1 ISU SAMPLE FABRICATION .....	18
2.1.1.2 NREL SAMPLE FABRICATION .....	19
2.1.2 STABILITY ISSUES OF PEROVSKITE SOLAR CELLS.....	20
2.2.1 DARK CAPACITANCE MEASUREMENT.....	22
2.2.2 CAPACITANCE SETUP .....	23
2.2.2.1 DARK CAPACITANCE FROM ISU SAMPLE.....	24
2.2.2.2 DARK CAPACITANCE FROM NREL SAMPLE.....	28
2.3 TIME-OF-FLIGHT MEASUREMENT .....	32
2.3.1 TOF EXPERIMENTAL SETUP .....	33
2.3.2 TIME-OF-FLIGHT.....	35
2.3.2.1 TOF MEASUREMENT OF ISU SAMPLE .....	36
2.3.2.2 TOF MEASUREMENT OF NREL SAMPLE .....	39
2.3.3 DRIFT MOBILITY DETERMINATION (WITH DISPERSION).....	40
2.3.4 TEMPERATURE DEPENDENCE .....	47
2.4 SUMMARY .....	49
<b>3. DISCUSSION AND PHYSICS IMPLICATIONS.....</b>	<b>52</b>
3.1: HALL EFFECT MEASUREMENT .....	53

3.2: THZ PHOTOCONDUCTIVITY MEASUREMENT.....	54
3.3: SPACE CHARGE LIMITED CURRENTS .....	56
3.4: A FINAL NOTE ON PEROVSKITES.....	58
<b>REFERENCES.....</b>	<b>60</b>

## TABLE OF FIGURES

Fig. 1: Perovskite crystal structure of molecular form $ABX_3$ , A: $CH_3NH_3$ , B: Pb, X: I. ....	2
Fig. 2: Flow chart of electron transport in DSSCs (not to scale). (1) light enters through the front contact and creates a conduction electron in the dye. (2) the electron drifts along the $TiO_2$ to the front contact where it is collected (3). (4) an electron is injected through the back contact into the electrolytic solution. (5) the solution dissociates with the extra charge and drifts towards the dye. (6) after the charge is neutralized on the dye, (7) the electrolytic solution becomes stable once again by combining. ....	4
Fig. 3: Structure of scaffolded PSCs. The oxide layer, which could be $TiO_2$ or $Al_2O_3$ , is represented by circles and the perovskite layer fills in the space between. ....	6
Fig. 4: Cartoon showing complete charge collection measured at times much greater than the transit time. ....	9
Fig. 5: Cartoon of photocurrents and photocharge distributions. ....	11
Fig. 6: Plot of drift mobility measurements made on $MAPbI_3$ by different groups ....	15
Fig. 7: Perovskite solar cell structures from ISU and NREL.....	18
Fig. 8: Experimental schematic of capacitance measurements. The sample "front" refers to the contact on the glass side and the sample "back" is the contact dot Au (Ag) for ISU (NREL) samples. Coaxial cables (50 $\Omega$ impedance) are used for connections between the pulser, sample, and digital oscilloscope). ....	24
Fig. 9: Transient charge collection in the dark at various applied bias $V_a$ , +0.2 V to -0.7 V (top to bottom) in steps of 0.1 V from ISU sample I3B1 at room temperature.....	26



Fig. 10: Total charge collected in the absence of illumination at 16  $\mu$ s after the initial response of the applied bias from ISU sample I3B1 at room temperature. The red dashed line is the linear fit of the data to determine the capacitance value from  $Q_{\text{dark}} = CV_a$  ..... 26

Fig. 11: Dark current fit (Eq. 2-4) with capacitance determined from Eq. 2-1 from the dark charge versus applied bias fit. The two curves are fitted to an exponential decay with parameter  $tRC = 69$  ns. Parameters used are  $C = 554$  pF,  $R = 125 \Omega$ . ..... 27

Fig. 12: Capacitance plotted from ISU sample I3B1 at various temperatures. Data was measured from 325K first and then in descending monotonic order. The red dashed line represents a linear fit of the capacitance over the temperature range yielding a slope of  $-0.72$  pF/K..... 27

Fig. 13: Transient charge collection in the dark at various applied bias  $V_a$ ,  $+0.8$  V to  $-0.8$  V (top to bottom) in steps of  $0.2$  V from NREL sample N3B2 at room temperature..... 29

Fig. 14: Total charge collected in the absence of illumination at 30  $\mu$ s after the initial response of the applied bias from NREL sample N3B2 at room temperature. Error bars are taken to be 10% of the recorded (average) value from the 100 samplings. The red dashed line is the linear fit of the data to determine the capacitance value from  $q_{\text{dark}} = CV_a$ . ..... 30

Fig. 15: Dark current NREL ..... 30

Fig. 16: Capacitance plotted from NREL sample N3B2 at various temperatures ..... 31

Fig. 17: SEM cross section image from NREL ..... 31

Fig. 18: Cartoon summary of the TOF process..... 33

Fig. 19: Schematic of the TOF experimental setup. .... 35

Fig. 20: Photocurrent transients for different applied reverse biases..... 36

Fig. 21: Photocharge transients and Hecht at room temperature from ISU..... 38

Fig. 22: Photocurrent transients for different applied biases at room temperature from NREL. . 39

Fig. 23: Photocharge transients at room temperature of NREL_930_3.....	40
Fig. 24: Photocurrent transient for different applied reverse biases. ....	43
Fig. 25: Drift-mobilities as a function of transit times.....	44
Fig. 26: Cartoon of photocurrents and photocharge distributions .....	46
Fig. 27: Temperature dependence of normalized charge transients. ....	47
Fig. 28: L/E vs. transit time plot of holes for a range of temperatures in V319_B2. ....	48
Fig. 29: Summary of temperature dependence of dispersion parameter and drift mobility .....	51
Fig. 30: Schematic of DC Hall measurement. ....	54
Fig. 31: Illustration of J-V relation of material exhibiting SCLCs without traps.....	57

## 1. Introduction

In this work, I found that the drift mobility in perovskite structured methyl ammonium lead iodide ( $\text{CH}_3\text{NH}_3\text{PbI}_3$  also abridged  $\text{MAPbI}_3$ ) to be of order  $10^{-1} \text{ cm}^2/\text{Vs}$ . I suppose this number doesn't really do it for most, and it shouldn't! In fact, at this point I expect most readers to be scratching their heads in confusion over several things mentioned here already. So, I suppose we shall start where most great (and some bad) stories do, with a little backstory.

As stated, I have studied a material called methyl ammonium lead iodide which is a truly interesting photovoltaic material used in solar cells given its rapid rise in efficiency over the past decade.<sup>1</sup> In 1839, calcium titanium oxide ( $\text{CaTiO}_3$ ) was discovered and given the name "perovskite". Though it was not until 1945 after X-Ray diffraction experiments<sup>2</sup> that it was confirmed to be the first mineral discovered to have a particular type of crystal structure. This crystal structure can be thought of as a superposition of face-centered and body-centered lattices with the molecular form of  $\text{ABX}_3$ , see Fig. 1. This structure is now known as perovskite. In the realm of high temperature ceramic superconductors, pseudo perovskite structures can be found such as yttrium barium copper oxide ( $\text{YBa}_2\text{Cu}_3\text{O}_7$ ).<sup>3</sup> The material methyl ammonium lead iodide is a mouthful, but since it has a perovskite crystal structure identical to  $\text{CaTiO}_3$ , the material I am studying will also be referred to as perovskite. I make the associations A:  $\text{CH}_3\text{NH}_3$ , B: Pb, X: I. What is perhaps more troublesome is that other researchers are attempting to find a substitute for lead with other metals and iodine with different halogens while they maintain the name: perovskite. Also, formamidinium based lead trihalides ( $\text{FAPbI}_3$ ) have taken some interest due to its lower bandgap energy.<sup>4,5</sup> For this current work, the term "perovskite" will always refer to

$\text{CH}_3\text{NH}_3\text{PbI}_3$ , unless stated otherwise. I will often use the abridged molecular form  $\text{MAPbI}_3$  to avoid confusion.

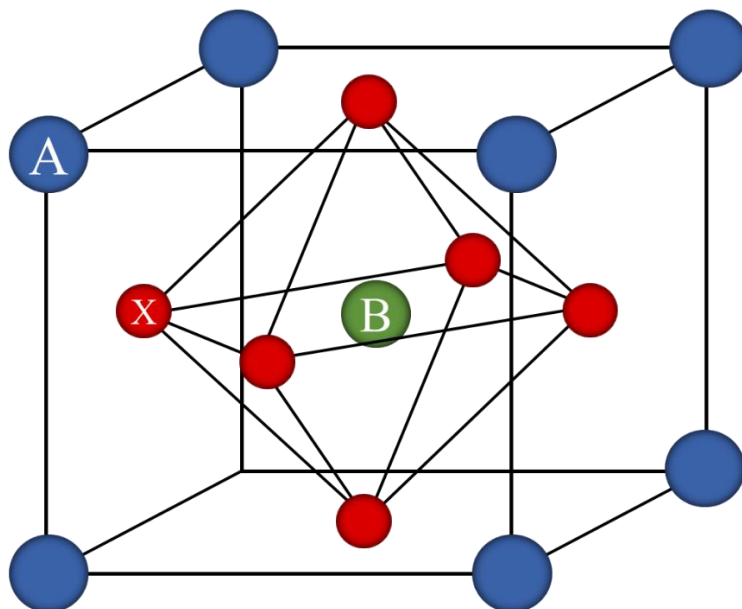


Fig. 1: Perovskite crystal structure of molecular form  $\text{ABX}_3$ , A:  $\text{CH}_3\text{NH}_3$ , B: Pb, X: I.

In this chapter I will discuss the motivation of studying the drift mobilities of this material and the implications it has for device makers. I shall start by telling the short, but rich, history of perovskite solar cells (PSCs). Then there will be a few words on drift mobility. I will then give a brief introduction to charge transport through the lens of a simple “normal” transport model which will be followed up with a more complex “dispersive” model. I will also provide a description of the time-of-flight (TOF) method used for observing transport phenomena in semiconductors. I will conclude this chapter by tying the relevance of my work to the bigger picture.

In the second chapter, the heart of the thesis is presented. This will include details on sample preparation, characterization, and the time of flight experiment used to determine drift mobilities

for both electrons and holes. I also present my data and discuss how spatially dispersive transport explains my observations.

In the last chapter, I discuss other research groups that used different techniques to measure a drift mobility for perovskite. These experiments are interesting in that some measure transport properties in the picosecond domain and yet are consistent with our measurements performed in the nanosecond domain. I conclude with a discussion on the direction of PSC research.

## 1.1. Perovskites rise to the spotlight

The progress of photovoltaics has been remarkable. Interest is driven primarily in solar cell technology, in particular, making devices more affordable in terms of price per Watt hour.

I will take some time to discuss dye sensitized solar cells (DSSCs) here only because PSCs were once made with sensitized cell structures. DSSCs, or Gratzel cells,<sup>6</sup> are characterized by their photosensitive dye which mimics the role of chlorophyll in plants. The structure of the cell consists of a transparent plastic or glass on top (light entering side) and bottom, this acts as an encapsulant to protect the cell from the environment, see Fig. 2. A transparent conducting oxide (TCO) layer acts as an anode and is the top contact. Beneath the TCO is usually a titanium dioxide ( $\text{TiO}_2$ ) “scaffold” structure to act as an electron transport medium as well as a semiconductor. The  $\text{TiO}_2$  is then soaked with a photosensitive dye, such as ruthenium-polypyridine. In a three-dimensional “scaffold” geometry, the amount of dye that can effectively create photoelectrons is greatly enhanced. An electrolyte is then dissolved into the “dye sensitized”  $\text{TiO}_2$  which restores missing electrons from the dye. Once the electrolyte donates the electron, it diffuses towards the back where a layer of platinum attached to a counter electrode

donates an electron to restore neutrality in the electrolyte. There is finally a back-contact layer which completes the circuit. The transport in  $\text{TiO}_2$  is ambipolar, meaning that a cloud of positive ionic charge follows in the electrons wake.<sup>7</sup> Disadvantages to these cells are numerous: low power conversion efficiencies, expensive chemicals and dyes, and volatile chemicals are often used. Work to solve some of these problems are ongoing.

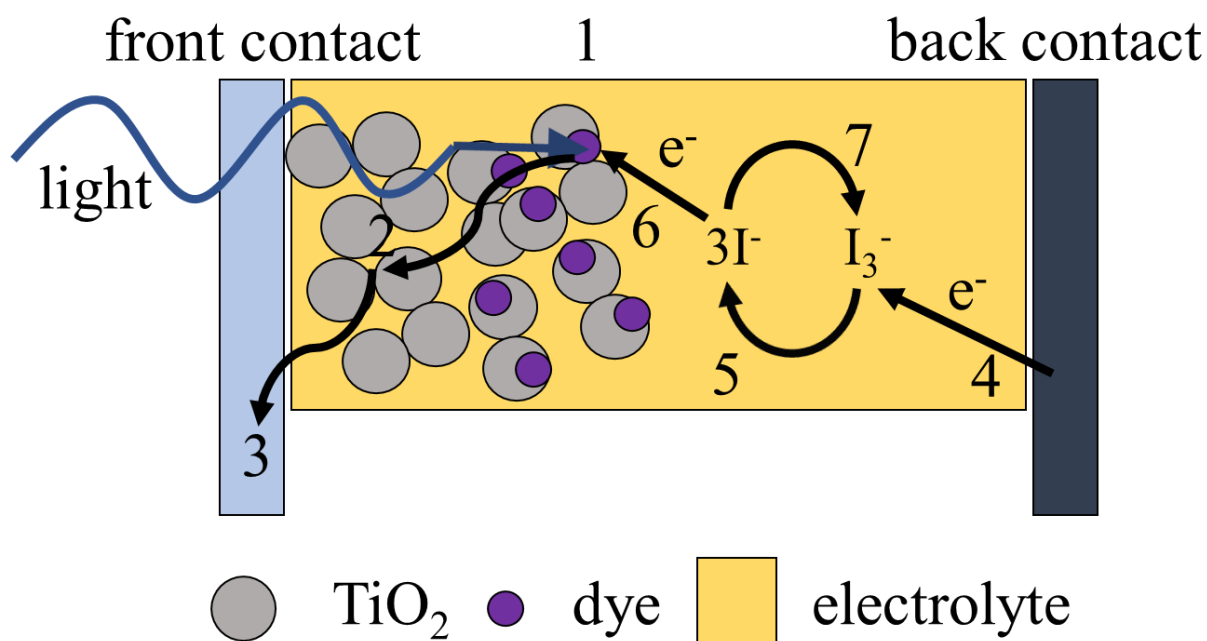


Fig. 2: Flow chart of electron transport in DSSCs (not to scale). (1) Light enters through the front contact and creates a conduction electron in the dye. (2) The electron drifts along the  $\text{TiO}_2$  to the front contact where it is collected (3). (4) An electron is injected through the back contact into the electrolytic solution. (5) The solution dissociates with the extra charge and drifts towards the dye. (6) After the charge is neutralized on the dye, (7) the electrolytic solution becomes stable once again by combining.

The inception of PSCs began in 2009 albeit with a power conversion efficiency of less than 4%,<sup>8</sup> but quickly rose with some ingenuity. Much of the seminal work on PSCs was presented during 2012 in two papers by Park *et al.*<sup>9</sup> and then Snaith *et al.*<sup>10</sup> which would help improve device stability, carrier lifetimes, and efficiency. Park substituted an electrolyte, which dissolved the

sensitizers over time, with a hole transport material (HTM) known as spiro-MeOTAD (2,2',7,7'-tetrakis(N,N'-di-p-methoxyphenylamine)-9,9'-spirobifluorene). This not only increased the stability of the power conversion efficiency, but increased the efficiency to just under 10%. Snaith showed that there were many things PSC researchers could be doing differently with their cell geometries and composition. First of these innovations implemented “mixed-halide” perovskites, substituting some of the iodine for chlorine, i.e.  $\text{MAPbI}_3$  to  $\text{MAPbI}_{3-x}\text{Cl}_x$ . This increased the carrier lifetimes and made the devices a bit more robust. Next was to simply coat perovskite on top of the nanoporous  $\text{TiO}_2$  “scaffold” layer, see Fig. 3. This allowed the PSCs to be made much thinner than had been done previously. It should be noted that the perovskites being used are thin film polycrystalline  $\text{MAPbI}_3$ . Snaith also found that replacing the  $\text{TiO}_2$  layer with an insulating aluminum oxide ( $\text{Al}_2\text{O}_3$ ) layer increased the open circuit voltage ( $V_{oc}$ ) and for the first time the efficiency for PSCs rose above 10%. Lastly, they demonstrated that PSCs must exhibit independent electron and hole transport behavior and removed the “scaffold” (sensitized) architecture completely. This led to the adoption of planar geometry PSCs which are studied in this dissertation, see Fig. 7. These papers provided the ground work for the surge of world record efficiencies of PSCs to date of this dissertation. For more information on the timeline of advancements in PSCs please refer to the National Renewable Energy Laboratory’s (NREL) “Best Research-Cell Efficiencies” chart<sup>11</sup> or discussion.<sup>12</sup> Currently the world record is held by KRICT (Korean Research Institute of Chemical Technology) with an efficiency of 22.7%.<sup>13</sup> It should be noted that these cells are not necessarily stable and stressed that these are research grade solar cells kept under ideal conditions. Another disclaimer is that the composition of PSCs from KRICT are thin film  $\text{FAPbI}_3$  type “perovskites”.

PSCs also have a unique property when measuring their current voltage characteristics, which determine solar cell efficiencies.<sup>14,15</sup> This property is dubbed “anomalous hysteresis” and can make the determination of high efficiency PSCs difficult by overestimating the open-circuit voltage, the voltage that is generated across the cell under open circuit conditions.<sup>16</sup> This is beyond the scope of this paper and will be not be further discussed.

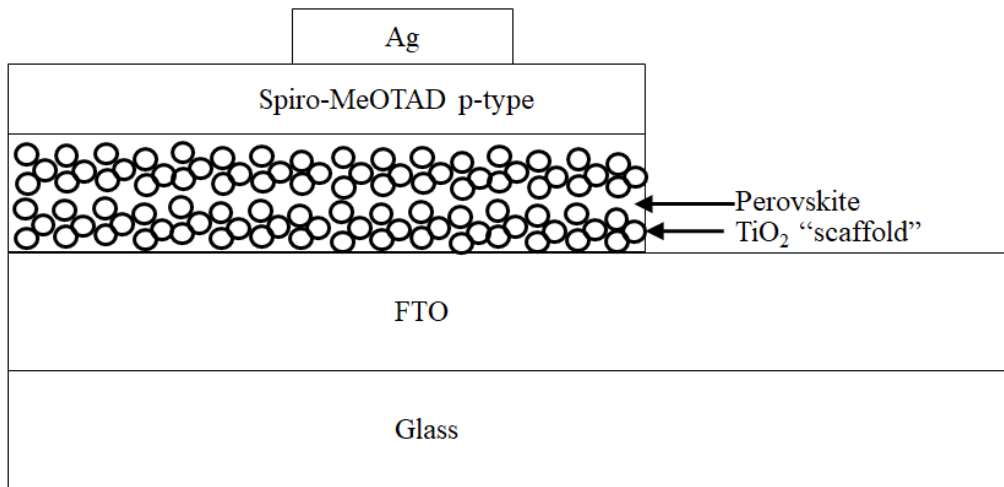


Fig. 3: Structure of scaffolded PSCs. The oxide layer, which could be TiO<sub>2</sub> or Al<sub>2</sub>O<sub>3</sub>, is represented by circles and the perovskite layer fills in the space between.

In terms of efficiency alone, PSCs rival other solar cell technologies that have been around for decades. For instance, copper indium gallium selenide (CIGS), cadmium telluride (CdTe), multi-crystalline silicon, and thin film silicon solar cells have all been surpassed by PSCs.

## 1.2. Drift Mobility

One of the intrinsic properties of a material is drift mobility. The drift mobility,  $\mu_D$ , is defined as the proportionality factor relating the drift velocity of charge carriers,  $v_D$ , to the electric field,  $E$ .



$$v_D = \mu_D E \quad (1)$$

The drift mobility is an important value that can have big implications for solar cell manufacturers, such as prescribing an ideal material thickness.<sup>17</sup> There have been a handful of techniques that can calculate some value that resembles a drift mobility, though often times in the literature, these values are simply labeled as an effective mobility. Such can be seen in transistor style measurements where the current travels laterally across a surface rather than through the surface, which risks unpredictable surface effects contaminating the data. For pure crystals, the Hall effect measurement is quite sufficient in identifying the majority carrier and identifying the value of the majority carrier's mobility. The Hall effect, however, is less clear when the minority carrier's mobility is of similar magnitude. There can be issues using this measurement for lower mobility materials which would require unreasonably large (greater than 10 T) magnetic fields to measure. However, ways to lessen the dependence on high magnetic fields using ac-fields and novel analysis do exist.<sup>18</sup> Application of this technique to PSCs has also been performed.<sup>19</sup> However, photo-carrier time-of-flight is a superior technique that is especially useful in the low mobility domain.

### 1.3. Normal and Dispersive Transport

I will be discussing two distinct transport models in this dissertation: normal and dispersive transport. I primarily use the normal transport model as a pedagogical approach for the underlying physics in PSCs. I will then discuss a slightly more involved, though relevant, extension of the normal transport model: the dispersive transport model.

### 1.3.1. Normal Transport Model

The normal transport model describes a sheet of moving charges through a medium that causes a displacement current in the circuit. The displacement current is defined by the change of the electric field with respect to time. This current diminishes when the charge carriers arrive at any electrode. The time it takes for the charge to cross the thickness of the medium is called a transit time,  $t_T$ . We call this normal transport only if the average drift velocity of the carriers is constant and we can define a clear transit time depending on the internal electric field.<sup>20</sup> To put it simply, the sheet of charge carriers travels from one end of the medium and drift with a constant velocity to the opposite end of the medium. Usually the sheet of charges diffuses as it travels causing a slight broadening of the sheet as it traverses the sample. Though, under low charge carrier densities this effect can be minimized and is negligible in my measurements. Since the sheet of charge is moving with a constant velocity, we can say that the position of the sheet,  $x(t)$ , is directly proportional to time,  $t$ .

$$x(t) \propto t \quad (2)$$

An analysis of transit times at different electric field densities will show that the drift mobility,  $\mu_D$ , will be constant as well, under modest applied bias. Increasing the applied bias too much can cause other undesired effects to occur.

For our present case, we simply need to check that all the charge carriers being measured are photo charge carriers. If this is the case then the charges collected should saturate at some sufficiently high bias. This saturation is due to the finite amount of photoelectrons generated from a short light pulse which drift across the cell quicker with greater applied bias. We call this photo charge saturation “complete charge collection” and denote it as  $Q_0$ , see Fig. 4. This is easy

enough to check for, we can simply shine a low intensity light pulse on the sample at progressively greater bias through the material until we see that the charge saturates past some bias. Going much further can cause other charge carriers in the sample to be freed and the ability to determine the mobility becomes much more complicated. I only used voltages on the order of the open-circuit voltage which was not sufficient to see this effect.

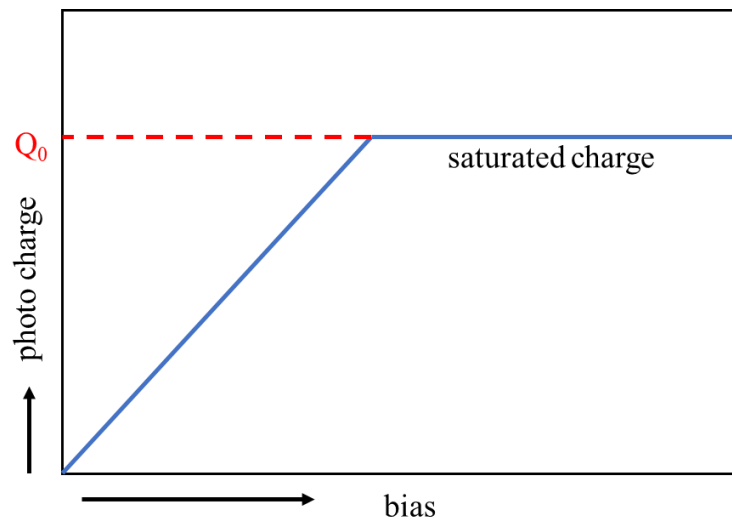


Fig. 4: Cartoon showing complete charge collection measured at times much greater than the transit time.

### 1.3.2. Dispersive Transport Model

In some disordered materials, charge transport is not sufficiently modeled by Eq. 2. The time dependence on the distance the sheet traveled becomes non-trivial and is proportional to a power dependent term. The power is called the dispersion parameter which we denote,  $\alpha$ .

$$x(t) \propto t^\alpha \quad (3)$$

The actual transport of these “sheets” of charge is curious, please refer to Fig. 5. The peak is localized at the site it was initially created in the medium and then spreads out until the charge is

collected. The calculation of the mobility is more involved and will be covered in detail in Chapter 2. Dispersive transport was investigated by Scher\* and Montroll in the 1970s.<sup>21</sup> They found that the early time current decreases much slower than later time current. In dispersive materials, the charge cannot technically be fully collected for any finite time. Though, for all intents and purposes, a negligible portion is left after a few transit times of collection. This is contrary to the normal transport case where the charge can be completely collected at finite times. For all intents and purposes, the current can diminish enough such that we can still define complete charge collection,  $Q_0$ , without any worries (i.e. after a few transit times have passed 99% of the charge is accounted for).

---

\* Harvey Scher received his Ph.D. from Syracuse University under Allen Miller studying many boson systems.

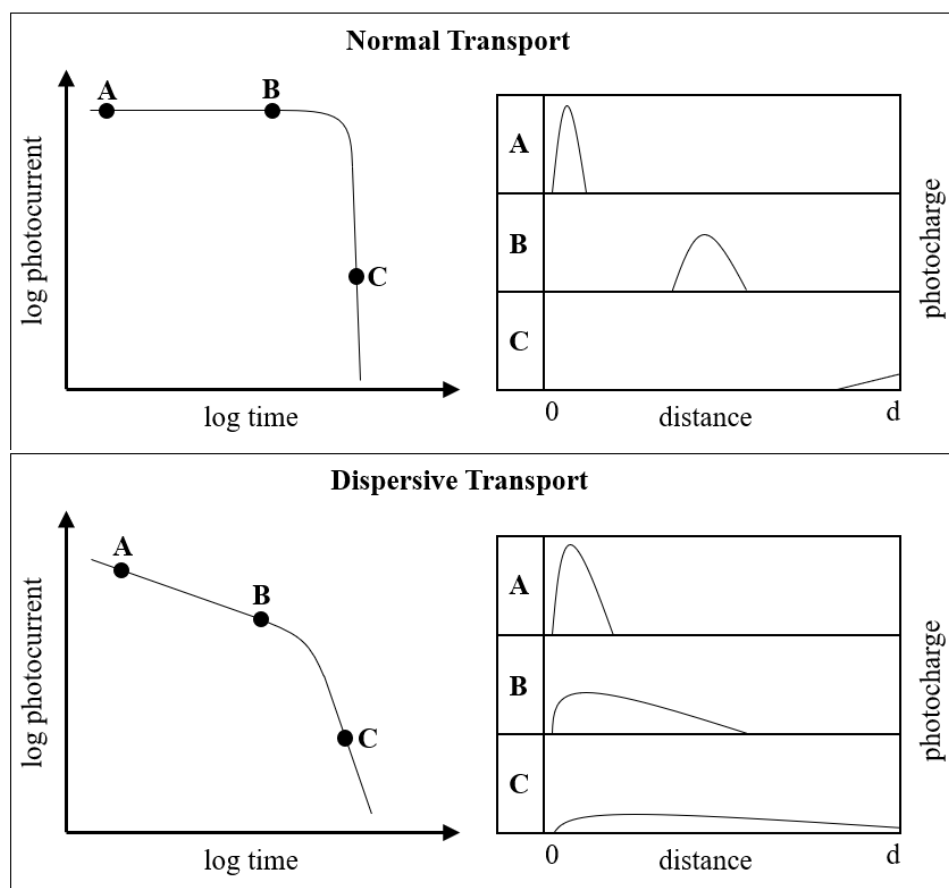


Fig. 5: Cartoon of photocurrents and photocharge distributions of normal (top) and highly dispersive, low  $\alpha$ , transport (bottom).

## 1.4. Time-of-Flight

The photo-carrier time-of-flight (TOF) measurement for semiconductors is straightforward compared to other types of measurements that involve transport phenomenon.<sup>22</sup> It relies upon a thin sheet of charge being created near the surface of the insulating semiconductor (in our case perovskite) and studying how the sheet of charge evolves with time under the influence of a constant electric field. Likewise, this is a transient measurement that allows sensitivity to directly observe phenomena associated with charge transport. The TOF measurement has several advantages over the aforementioned methods because it is a purely electrical measurement with

charges flowing through the material normal to the contacts, so there is no need for magnetic fields and excludes surface effects. Analysis of TOF data can also tell us about the physics of charge transport in the material, including information on traps and whether the material has more exotic properties such as time dependent drift mobilities.<sup>29,23</sup>

The TOF measurement for solar cells involves creating a sheet of drifting photocharges that propagate through a material from an externally applied electric field,  $E$ . From there a transit time is measured,  $t_T$ , which corresponds to the average displacement of the sheet of charges to traverse half the thickness of the perovskite,  $L$ , for some constant  $E$ . These photocharges are created using a monochromatic light source. For normal transport, these quantities are then related by the following expression:

$$\frac{L}{E} = \mu_D t_T. \quad (1-4)$$

The choice of wavelength for the light source is important and depends on the material's absorption coefficient, a measure of the ability for the MAPbI<sub>3</sub> to absorb light at specific frequencies. Usually a quantum efficiency (QE) measurement is performed to show how much absorption occurs at different wavelengths of light. A QE measurement gives a ratio of how many photocharges contribute to the current in a material per absorbed photon. Coupled with the absorption coefficient, this information allows the experimenter to control how far into the sample that the sheet of photocharges is created, i.e. light with lower absorption coefficients will penetrate deeper into the sample whereas light with high absorption coefficients will mostly be absorbed near the surface. Since the absorption of a photon creates an electron-hole pair, the absorption depth can also help the experimenter select a carrier for measurement.

The information from this experiment is displayed on an oscilloscope which measures the voltage change from the displacement current of the moving photocharges in the material across

the circuits resistance. This is a little confusing so I will take some time to explain. When the photocharges are created inside the material and start to drift across the sample, they induce a displacement current which is what causes the voltage on the oscilloscope to give us information. The displacement current,  $J_d$ , is the change in the electric field with respect to time across the sample and is defined in Eq. 4, where  $\epsilon$  is the electric permittivity inside the material.

$$J_d = \epsilon \frac{\partial E}{\partial t} \quad (1-5)$$

The displacement current density is related to the displacement current,  $i_d$ , and the area through which the charge flows,  $A$ :  $J_d = i_d / A$ . The term displacement current will not be used for the remainder of this dissertation and will simply be referred to as the photocurrent. The photocurrent,  $i_{photo}$ , is defined by the current generated in the dark,  $i_{dark}$ , subtracted from the current generated under illumination,  $i_{light}$ :

$$i_{photo} = i_{light} - i_{dark} \quad (1-6)$$

For dispersive transport,  $i_{photo}$  has a particular time dependence described by Eq. 1-7 and Eq. 1-8:<sup>21</sup>

$$i_{photo} = i_0(t/t_T)^{-(1-\alpha)} \text{ for } (t \leq t_T) \quad (1-7)$$

$$i_{photo} = i_0(t/t_T)^{-(1+\alpha)} \text{ for } (t > t_T) \quad , \quad (1-8)$$

where  $i_0$  is a common proportionality constant.

These equations complicate the expression of  $\mu_D$  and cause a bit of confusion when trying to declare it as a specific value due to its dependence on  $L/E$  which I shall discuss in more detail at the end of Chapter 2.

## 1.5. Thesis Relevance

The measurement performed in this thesis is the first temperature dependent transient study of MAPbI<sub>3</sub>. I am by no means the first person to report a drift mobility,  $\mu_D$ , for this material,<sup>24,25,26,27,28</sup> though I am the first to discover the spatially dispersive nature of this material.<sup>29</sup> A summary of measurements made on this material can be found in Fig. 6.



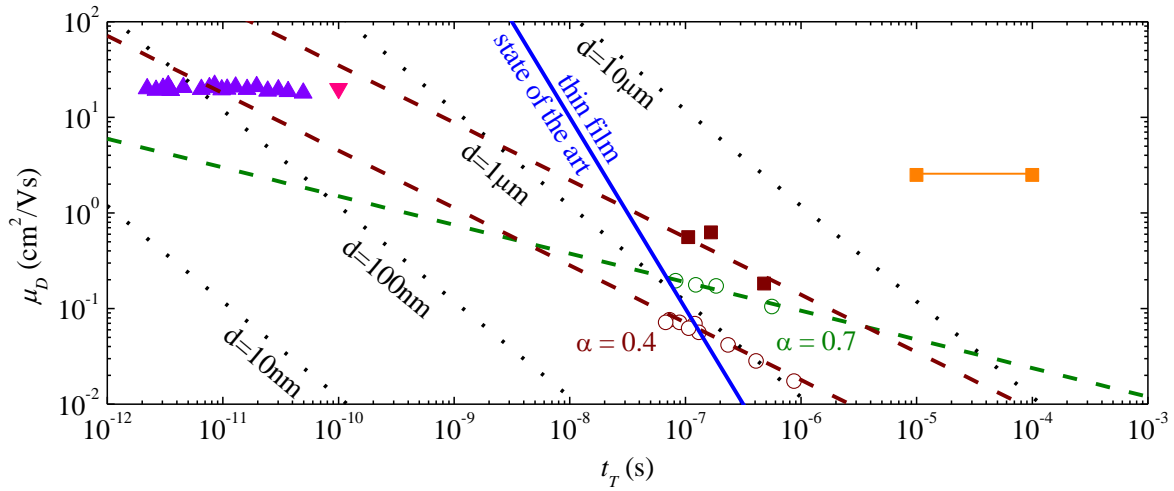


Fig. 6: Plot of drift mobility measurements made on MAPbI<sub>3</sub> by different groups. The solar cell operation zone is based on a “displacement” field measurement which relates the absorber layer thickness to the electric field inside the cell. The solid blue line represents the optimal conditions for solar cell operation<sup>30</sup> calculated using values<sup>31</sup> from current state of the art MAPbI<sub>3</sub> thin film solar cells. Purple triangle (both carriers)<sup>27</sup>, pink triangle (both carriers)<sup>28</sup>, maroon and green open circles (holes) and solid maroon squares (electrons)<sup>29</sup>, orange line (no distinct carrier specified)<sup>26</sup>. Dotted lines are for visual reference and assume constant photogeneration rates. Blue solid line shows state of the art cell under operating conditions assuming constant photogeneration rate and operating voltage.

The information in Fig. 6 warrants discussion. This figure is an attempt to summarize the importance of the measurements made in this thesis. The blue solid line represents optimal operation conditions using a space charge limited calculation which is derived from Schiff.<sup>30</sup>

$$\mu_D = \left( \frac{4\epsilon\epsilon_0 d}{9J_{sc}} \right) t_T^{-2} \quad (1-9)$$

In Eq. 1-9,  $\epsilon\epsilon_0$ , represents the relative permittivity,  $d$  represents the MAPbI<sub>3</sub> thickness,  $J_{sc}$  is the short-circuit current density, and  $t_T$  is the average time it takes the photocharge carriers to traverse halfway through the sample. The numbers used in the calculation were taken from current state-of-the-art solar cells under operating conditions with  $J_{sc} = 21.8 \text{ mA/cm}^2$  and  $d = 310 \text{ nm}$ .<sup>31</sup> It is quite fortunate that the time domain of our measurement precisely overlaps with these conditions. The dotted lines represent constant thickness lines given by Eq. 1-10:

$$\mu_D(t_T) = \frac{d^2}{2\left(\frac{2}{3}V_{OC}\right)t_T} \quad (1-10)$$

The factor of  $2/3 V_{OC}$  represents an estimate for the operating voltage for a cell that is maximizing its power output. For these lines we use the value for state of the art for thin film MAPbI<sub>3</sub> solar cells,  $V_{OC} = 1.12\text{V}$ .<sup>31</sup>

I have included some other measurements as well, though Ponseca *et. al.* and Wehrenfennig *et. al.* use THz techniques to make their measurements on single crystal MAPbI<sub>3</sub>. The THz measurements are not made on solar cell devices and also cannot distinguish between carriers. Shi *et. al.* uses space charge limited currents and also single crystal, and never claims what carrier they are measuring. My measurements were performed on thin film perovskites with both carrier types being measured. I found that the thin films were dispersive, which is represented by the dashed lines in Fig. 6. This dispersion is most likely a consequence of spatial disorder which will be discussed in the following chapters.

## 2. Characterization and Measurements of Perovskite Solar Cells

### 2.1 Fabrication and Device Characterization

In this section I will describe how the PSCs from the National Renewable Energy Laboratory (NREL) and Iowa State University (ISU) were made and delivered to Syracuse University. I will also describe some early characterizations of the cells and some

#### 2.1.1 Fabrication

Thin film perovskite solar cells are typically made with a “superstrate” architecture in which light enters through the glass substrate. The cell itself is an n-i-p or p-i-n planar heterojunction with the perovskite acting as the intrinsic, “i”, layer. High efficiency cells typically use perovskite thicknesses on the order of 500 nm; however, for our time-of-flight measurements, cells around 1000 nm thicknesses were used to combat issues with the electronic rise time,  $t_{RC}$ . Increasing the thickness halves the capacitance (for a given cell area), and at the same time it increases the transit time for carriers (at a given electric field).

In the literature, the p-layer is typically called the hole-transporting material (HTM).

Perovskite thin films are typically fabricated using one of two processes: solution processing, which can be further broken down into spin coating or spray processing; and vapor processing. The cells from National Renewable Energy Laboratory (NREL) were prepared via spin coating and the cells at Iowa State University (ISU) were prepared via vapor processing. Both cells were superstrate n-i-p planar heterojunction cells, see Fig. 7.

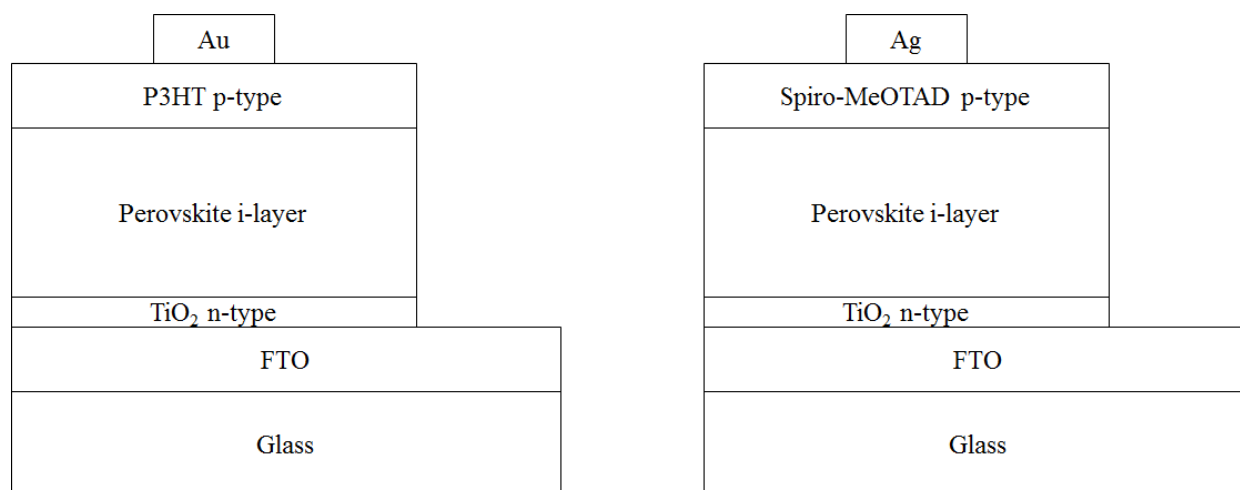


Fig. 7: Perovskite solar cell structure from ISU (left) and NREL (right). Light is incident through the FTO-coated glass.

### 2.1.1.1 ISU sample fabrication

Samples from ISU were prepared at the Microelectronics Research Center. The process starts with a fluorine-doped tin-oxide (FTO) coated glass substrate; FTO is a transparent conducting oxide material. FTO-coated glass was purchased from several vendors. An additional thin layer of titanium dioxide (TiO<sub>2</sub>) on the FTO which acts as the n-layer is also present. Lead iodide (PbI<sub>2</sub>) is then thermally evaporated under vacuum onto the TiO<sub>2</sub> layer. From here the substrate is transported into a high density grade graphite vessel with methyl-ammonium-iodide (CH<sub>3</sub>NH<sub>2</sub>I or MAI) which is inside a nitrogen glovebox. The vessel is heated such that the interior of the chamber reaches ~150 °C at which the MAI turns to vapor and interacts with the PbI<sub>2</sub> until the color of the film turns from yellow to dark brown, which indicates the formation of perovskite. From here the substrate is kept for one to two days under vacuum (10<sup>-6</sup> torr) at room temperature to remove excess MAI. Undoped poly-3-hexylthiophene (P3HT) in a chlorobenzene solution is then spin-coated onto the perovskite layer resulting in the p-type heterojunction. Finally, gold

(Au) is thermally evaporated as a back contact layer. More details of the process can be found in Abbas, *et al.*<sup>32</sup>

### 2.1.1.2 NREL sample fabrication

As with the samples from ISU, NREL also prepared a superstrate n-i-p cell with TiO<sub>2</sub>/FTO/glass substrate, where the TiO<sub>2</sub> layer was deposited using spray pyrolysis, a technique that deposits the material onto a substrate in a liquid phase while the substrate itself is heated, at 450 °C. The perovskite is created via solution processing and deposited by spin coating. To start, 24 mL of 33 wt% of methyl-ammonium (CH<sub>3</sub>NH<sub>2</sub> or MA) solution in anhydrous ethanol is reacted with 10 mL of 57 wt% of hydrogen iodide (HI) in water, in a 100 mL ethanol solvent contained at room temperature in a dry argon atmosphere. Once the reaction has taken place, the solvent is removed using a rotary evaporator leaving a MAI powder. From here a solvent-solvent extraction (SSE) method is utilized. This method uses PbI<sub>2</sub> and the previously made MAI at a 1:1 molar ratio in N-methyl-2-pyrrolidone (NMP). The solution is then spin-coated on the TiO<sub>2</sub> layer of the substrate and then dipped into a 50 ml bath of anhydrous diethyl ether (C<sub>2</sub>H<sub>5</sub>OC<sub>2</sub>H<sub>5</sub> or DEE) until the film turned brown. The substrate was then quickly dried by blowing N<sub>2</sub> gas on the substrate at room temperature in an environment kept at 30% relative humidity.

The selected HTM layer is made up of 1 mL chlorobenzene solvent, 30 µL 4-tert-butylpyridine (TBP), 30 µL bis(trifluoro-methane) sulfonimide lithium salt stock solution (500 mg Li-TFSI in 1 mL acetonitrile), and 80 mg 2,2',7,7'-tetrakis(N,N'-di-p-methoxyphenylamine)-9,9'-spirobifluorene (spiro-MeOTAD). The solution was deposited via spin-coating at room temperature in an atmosphere with less than 10% humidity. More details of the process can be

found in Zhou *et al.*<sup>33</sup> The samples are then shipped to Syracuse University where 120 nm thick silver contacts are deposited via thermal evaporation with a mask.

### 2.1.2 Stability issues of Perovskite Solar Cells

We will briefly describe current-voltage ( $I$ - $V$ ) measurements, though it is more practical to interpret data represented as current density-voltage ( $J$ - $V$ ) measurements. In  $J$ - $V$  measurements the area of the cell is invariant and the results can be easily scaled for any contact area.

$$J(V) = \frac{I(V)}{A} \quad (2-1)$$

Solar cells behave like diodes in the dark. That is, under reverse bias only negligibly small current exists, i.e. current is blocked from flowing across the cell in the direction of the applied bias due to internal space charge regions at the p and n junctions. Conversely in forward bias, the applied field favors the direction of the internal field and current can flow freely.

Analysis of  $J$ - $V$  curves for illuminated solar cells allow for the determination of several key parameters in determining the quality of the devices. The first of these is the open-circuit voltage,  $V_{OC}$ , which is the voltage at which no current flows through the device,  $I(V)=0$ .

Perovskites have had many issues affecting the stability of their performance. Such problems involve time, exposure to humidity, oxygen, high vacuum, and long exposure to ultra violet light in some instances.<sup>34</sup> We monitored the state of the cells principally by measuring the open-circuit voltage from the cells under a solar simulator (Newport Solar Simulator model: 91159). This parameter was actually measured using a sweep of the current  $I$  through the sample as a function of the applied voltage  $V$ .

Cells that were used for this study were sent overnight from their respective labs, ISU and NREL, inside a dry nitrogen filled capsule. This capsule was opened in air, and the open-circuit voltages of the cells on the several substrates were measured. One substrate was selected for further study and transferred to a vacuum cryostat. The remaining substrates were stored in the original capsule under dry nitrogen. A few minutes of exposure to air had less than a 0.01 V effect on the open-circuit voltage. In addition, we compared the  $V_{oc}$  before and after measurements in the cryostat, and these also showed no change in  $V_{oc}$  larger than 0.01 V. The aforementioned process was later replaced by a greatly simplified procedure that involved immediately measuring the  $I$ - $V$  characteristics under illumination to determine which of the several cells on each substrate had the highest  $V_{oc}$ . The open circuit voltage acts as an initial quality test of the solar cell important for TOF, discussed below. After this characterization, the samples were put under vacuum for the remainder of the experiment. Samples reported in this thesis experienced only small decreases in  $V_{oc}$ ,  $\sim 0.05$  V, after the TOF measurements were performed, sometimes over the course of five days. Some samples kept under vacuum experienced minimal change in  $V_{oc}$  over the course of a month, though they had minimal light exposure. A summary of some of these cells is reported in Table 1. Large differences in  $J_{sc}$  are due to calibration differences between NREL's equipment and Syracuse's. The light of the illuminator at Syracuse was certainly less intense.

	Measured on 8/27 → Measured on 9/3,4,5 resp.		
	NP1105_1	NP1105_2	NP1105_3
$J_{sc}$ (different due to calibration) (mA/cm <sup>2</sup> )	16.7 → 12.1	14.8 → 3.7	17.5 → 8.33
$V_{oc}$ (V)	0.90 → 0.79	0.85 → 0.72	0.91 → 0.75
Fill Factor	0.56 → 0.45	0.56 → 0.49	0.62 → 0.43

Table 1: Comparison of samples pre-shipment and post-shipment from NREL with errors less than 2%.

### 2.2.1 Dark Capacitance Measurement

In the time-of-flight method we ideally track a distribution of charges traversing an absorber layer of thickness  $d$ . The time-of-flight analysis requires knowledge of the thickness as an input in order to obtain a mobility. Presuming the dielectric constant of the material is known, capacitance measurements can electronically determine this thickness, which in the case of a light sensitive material, must be performed in the dark. For a n-i-p structure, we achieve this by taking advantage of the following two equations:

$$C = Q_{dark}/V_a \quad (2-2)$$

$$C = \frac{\epsilon\epsilon_0 A}{d} \quad (2-3)$$

where  $C$  is the capacitance,  $Q_{dark}$  is the magnitude of the charge in the p and n layers,  $V_a$  is the applied bias,  $\epsilon$  is the relative permittivity ( $\sim 18$  for thin film perovskite)<sup>35</sup>,  $\epsilon_0$  is the vacuum permittivity, and  $A$  is the area of the sample. The first task is finding the value of  $C$ , which can be determined by applying a voltage bias pulse and measuring the total charge that flows in the bias



circuit following application of the pulse. In practice, the dark current,  $i_{dark}$ , is measured and then integrated over time to determine the total charge.

$$q_{dark}(t) = \int_0^t i_{dark}(t') dt' \quad (2-4)$$

$$\lim_{t \gg t_{RC}} q_{dark}(t) = Q_{dark} \quad (2-5)$$

Here we write that  $Q_{dark}$  is independent of time for a large integration time, which is valid because the value of the current falls to negligible amounts exponentially after the initial applied bias is turned on:

$$i_{dark}(t) = i_{dark,0} \exp(-t/RC), \quad i_{dark,0} = V_a/R \quad (2-6)$$

where  $i_{dark,0}$  is the initial current response and  $RC$  is the resistance-capacitance product which is an important parameter called the electronic rise time, often denoted as  $t_{RC}$ .

Now that  $Q_{dark}$  is known it is possible to determine  $C$  and hence the thickness,  $d$ , of the sample using Eq. 2-2 and Eq. 2-3.

## 2.2.2 Capacitance Setup

A schematic of the dark capacitance experiment can be found in Fig. 8. We start our experiment by attaching probes to the front (FTO) and back (Au or Ag) contact of the cell, which is typically inside a cryostat evacuated to  $\sim 10^{-3}$  torr with a mechanical pump. We are careful not to evacuate to lower pressures as our cell fabricators have warned that this may cause faster degradation of the cells. We also monitor and control the temperature using a Lakeshore 321 Temperature Controller and liquid nitrogen. The liquid nitrogen cools the sample in the cryostat via conduction through copper contacts. Since the copper contacts the glass side of the sample, we

used vacuum grease between the glass and copper to ensure thermal contact. The front and back contacts are then attached to a LeCroy 9350CM 500MHz oscilloscope via coaxial cables. We synchronize a DC voltage pulse from our voltage pulser (Avtech AV-1015-B) to the trigger of the oscilloscope and output our voltage pulse to the front contact of our sample at CH2 on the oscilloscope. The voltage generator produces a constant DC pulse signal which is on for  $\sim 100 \mu\text{s}$  a rate of 1 Hz. This process is repeated for 100 cycles to average out random noise in the signal. The signal is then sent to a computer for data analysis.

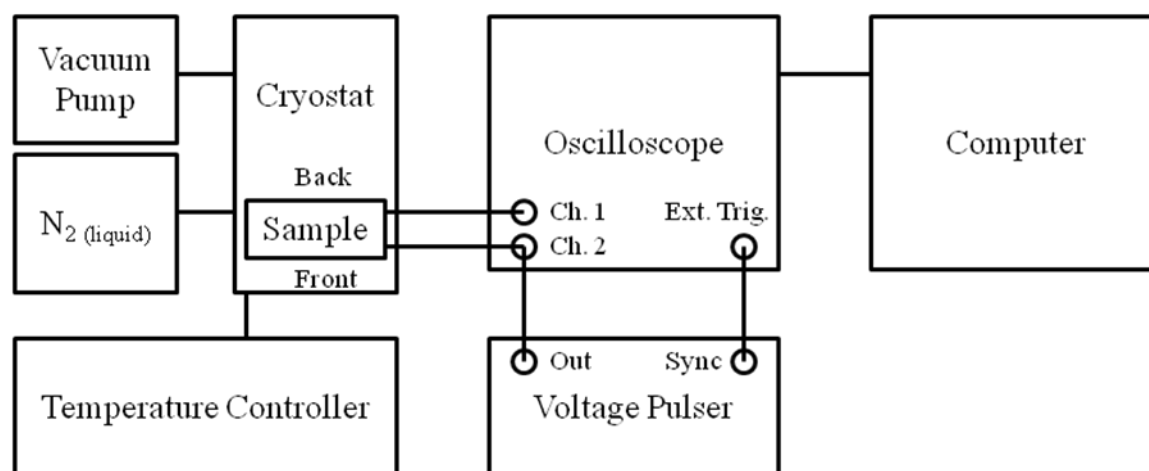


Fig. 8: Experimental schematic of capacitance measurements. The sample "front" refers to the contact on the glass side and the sample "back" is the contact dot Au (Ag) for ISU (NREL) samples. Coaxial cables ( $50 \Omega$  impedance) are used for connections between the pulser, sample, and digital oscilloscope).

### 2.2.2.1 Dark Capacitance from ISU Sample

The perovskite solar cell samples received from Iowa State (ISU)  $\text{MAPbI}_3$  thicknesses were initially determined during fabrication and reported to our lab along with the shipment of the samples. Back contacts were prepared at ISU and upon arrival were found to be irregularly shaped, best attempts at area estimates for the sample described in this section are between  $0.038\text{-}0.045 \text{ cm}^2$ . The thickness of the perovskite layer determined during fabrication of the sample was reported to be  $1.2 \mu\text{m}$ . The dark charge,  $q_{\text{dark}}$ , of the sample was determined from the

integration of the dark current,  $i_{dark}$ , measured at a given  $V_a$ , see Fig. 9. The charge does not look like it is being collected fast enough for larger  $V_a$ , however, at long enough times ( $t > 12 \mu\text{s}$ ) the charge remains constant and  $Q_{dark}$  can be determined. In Fig. 10,  $Q_{dark}$  is plotted against the applied bias and a linear fit is performed to determine the capacitance from Eq. 2-2. Using the value of capacitance, and a literature value of 18 for the relative dielectric constant, we estimate that the thickness of the perovskite layer is between  $1.1 \mu\text{m}$  and  $1.3 \mu\text{m}$  with the range stemming from the uncertainty in the area.

In Fig. 11, this capacitance is used to determine a goodness of fit to the time dependent dark current originally measured ( $i_{dark}(t) = i_{dark}(0) \exp(-t/t_{RC})$ ). The resulting time constant is also determined,  $t_{RC} = 69 \text{ ns}$ . We expect that  $t_{RC} = RC$ , from which we infer that  $R = 125 \Omega$ . Since the electronics contributes  $100 \Omega$  (50 for the pulser and 50 for the oscilloscope), it came as a surprise that  $25 \Omega$  was due to the solar cell. This resistance contributes to  $t_{RC}$  and limits our ability to measure signals that approach this value. The value is presumably due to connections to the cell, but we did not determine its precise origin.

We have performed this procedure at all temperatures used to determine drift mobilities and report our measurements in Fig. 12. There appears to be a small decrease in capacitance with a rise in temperature.

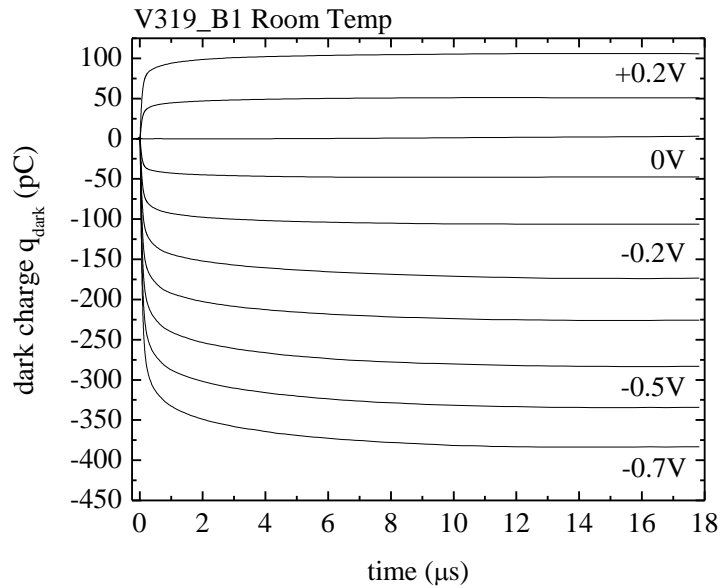


Fig. 9: Transient charge collection in the dark at various applied bias  $V_a$ , +0.2 V to -0.7 V (top to bottom) in steps of 0.1 V from ISU sample I3B1 at room temperature.

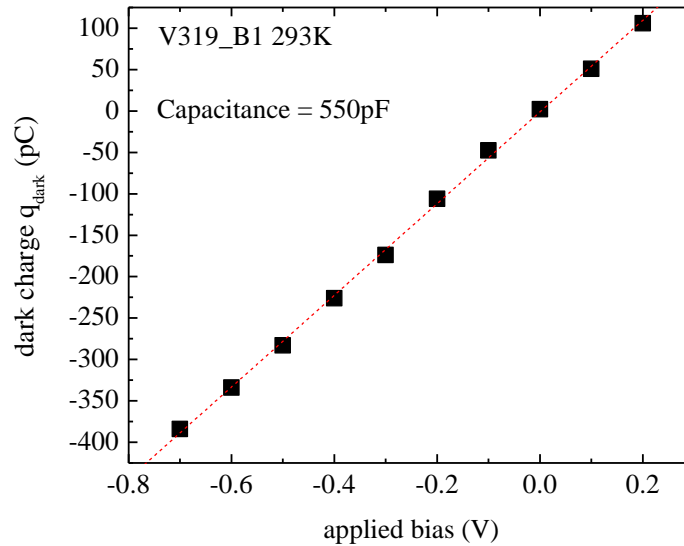


Fig. 10: Total charge collected in the absence of illumination at 16  $\mu\text{s}$  after the initial response of the applied bias from ISU sample I3B1 at room temperature. The red dashed line is the linear fit of the data to determine the capacitance value from  $Q_{\text{dark}} = CV_a$ .

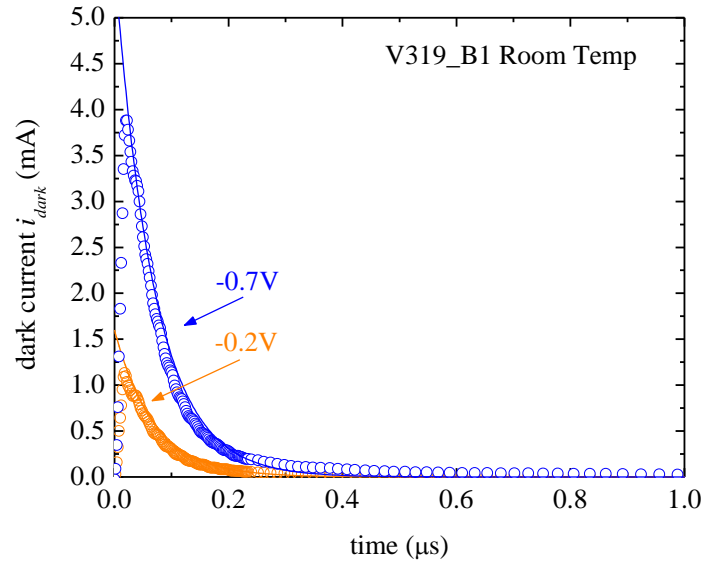


Fig. 11: Dark current fit (Eq. 2-4) with capacitance determined from Eq. 2-1 from the dark charge versus applied bias fit. The two curves are fitted to an exponential decay with parameter  $t_{RC} = 69$  ns. Parameters used are  $C = 554$  pF,  $R = 125$   $\Omega$ .

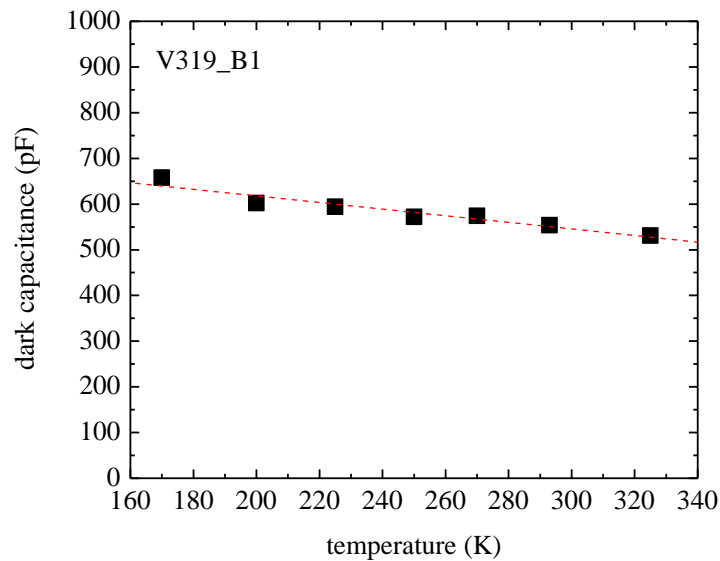


Fig. 12: Capacitance plotted from ISU sample I3B1 at various temperatures. Data was measured from 325K first and then in descending monotonic order. The red dashed line represents a linear fit of the capacitance over the temperature range yielding a slope of  $-0.72$  pF/K with an error of  $0.095$  pF/K.

### 2.2.2.2 Dark Capacitance from NREL Sample

The perovskite solar cell samples received from the National Renewable Energy Laboratory (NREL) thicknesses were also initially determined during fabrication and reported to our lab along with the shipment of the samples. Back contacts were prepared at Syracuse University and immediately upon arrival sample areas of  $0.031 \text{ cm}^2$  were made. The thickness of the perovskite layer determined during fabrication of the sample was reported to be  $0.8 \text{ }\mu\text{m}$ . The dark charge,  $q_{dark}$ , of the sample was determined from the integration of the dark current,  $i_{dark}$ , measured at a given  $V_a$ , see Fig. 13. Once again the charge does not look like it is being collected fast enough for larger  $V_a$ , however, at long enough times ( $t > 25 \text{ }\mu\text{s}$ ) the charge remains constant and  $Q_{dark}$  can be determined. In Fig. 14,  $Q_{dark}$  is plotted against the applied bias and a linear fit is performed to determine the capacitance from Eq. 2-2.

In Fig. 15, the capacitance value found using the total dark charge is used to determine a goodness of fit to the time dependent dark current originally measured. As can be seen in the figure, the fit parameters predicts the time dependence of the dark current well. We report an even higher resistance through the solar cell of  $40 \text{ }\Omega$ , however. Using the value of capacitance we verify that the thickness of the sample is  $0.8 \text{ }\mu\text{m}$ . The resulting time constant is also determined,  $t_{RC} = 88 \text{ ns}$ .

We have performed this procedure at all temperatures used to determine drift mobilities and report our measurements in Fig. 16. There appears to be a small increase in capacitance with a rise in temperature, contrary to what was found in the ISU sample. These findings should be further investigated in the future to determine if the change in capacitance is real. Our

collaborators from NREL have also provided an SEM image verifying their determined thickness from fabrication of from a 950 nm thick sample, Fig. 17.

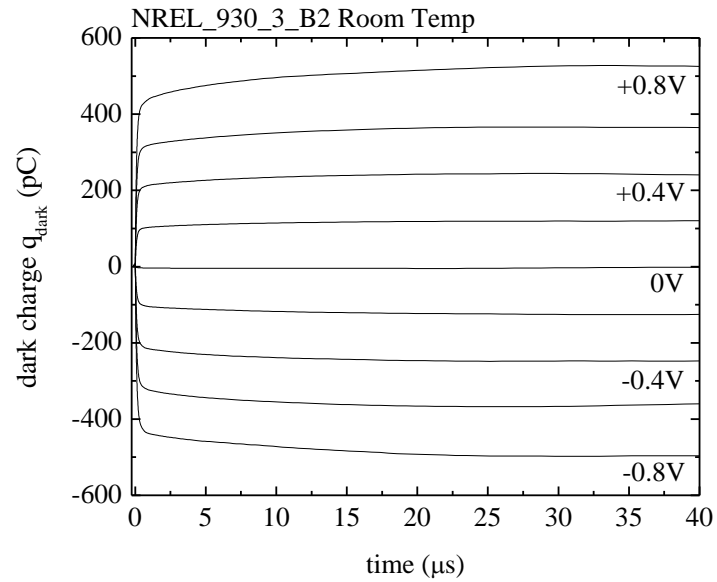


Fig. 13: Transient charge collection in the dark at various applied bias  $V_a$ , +0.8 V to -0.8 V (top to bottom) in steps of 0.2 V from NREL sample N3B2 at room temperature.

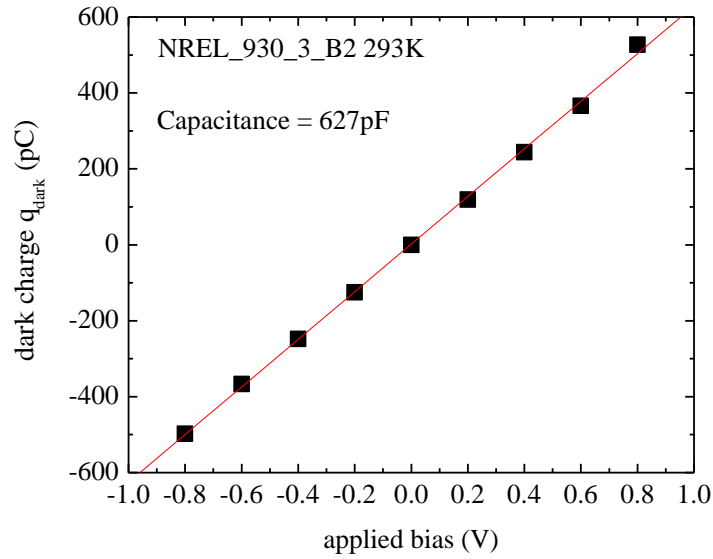


Fig. 14: Total charge collected in the absence of illumination at  $30 \mu\text{s}$  after the initial response of the applied bias from NREL sample N3B2 at room temperature. The red dashed line is the linear fit of the data to determine the capacitance value from  $q_{dark} = CV_a$ .

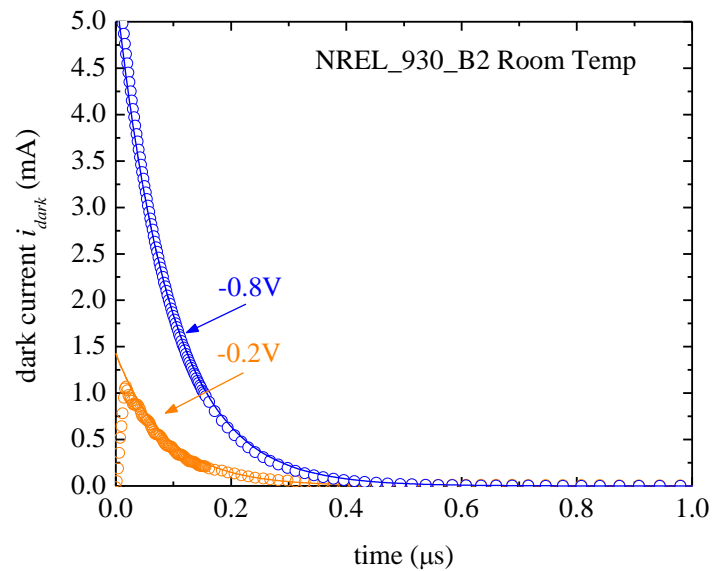


Fig. 15: Dark current fit (Eq. 2-4) with capacitance determined from Eq. 2-1 from the dark charge versus applied bias fit. Parameters used are  $C = 627 \text{ pF}$ ,  $R = 140 \Omega$ , and  $V = -0.2 \text{ V}$  (orange) and  $-0.8 \text{ V}$  (blue). The associated  $t_{RC}$  is thus  $88 \text{ ns}$ .



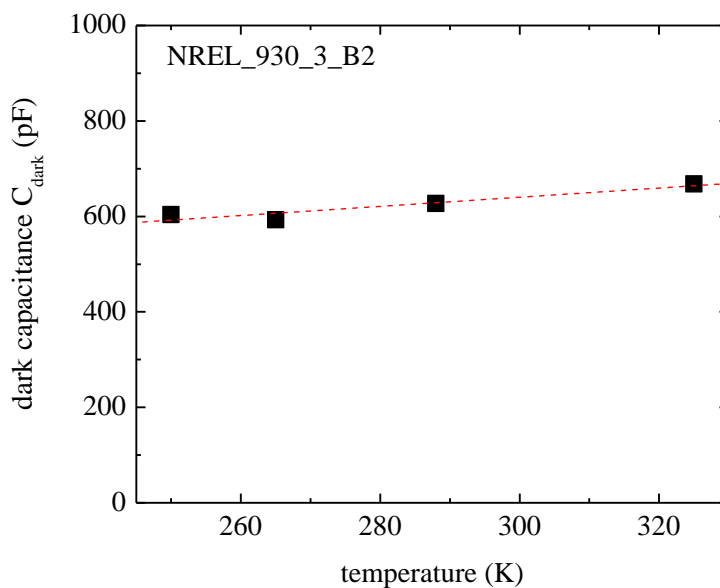


Fig. 16: Capacitance plotted from NREL sample N3B2 at various temperatures. Data was measured from 325 K first and then in descending monotonic order. The red dashed line represents a linear fit of the capacitance over the temperature range yielding a slope of +0.96 pF/K with an error of 0.23pF/K.

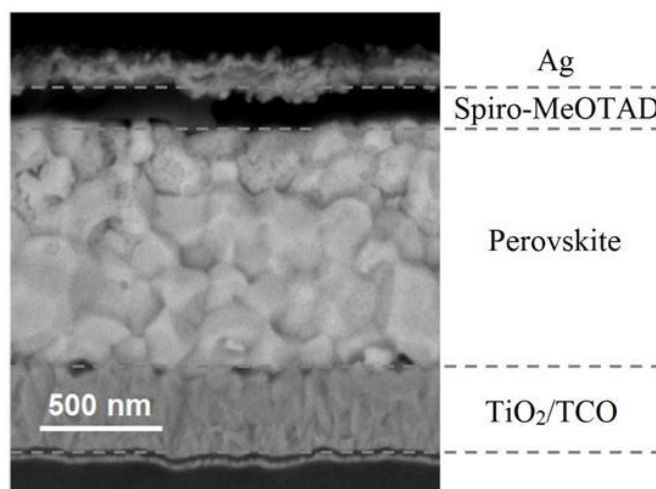


Fig. 17: SEM cross section image from NREL verifying the thickness of the determined value from fabrication, 1.0  $\mu\text{m}$  for this sample.

## 2.3 Time-of-Flight Measurement

There are several experimental methods to determine the drift mobility of charge carriers in a semiconductor, as was discussed in Chapter 1. For this dissertation, I use a photocarrier time-of-flight (TOF) measurement which is preferable to determine the drift mobility of a semiconductor because it allows for time dependent analyses and is quite straight forward in terms of the underlying physics.

For TOF, a sheet of charges is typically generated at the surface of the semiconductor which then drifts via an applied electric field,  $E_a$ , across the semiconductor to a back contact where the charges are collected. It is important that the sheet of charges generate a negligible electric field compared to the applied field. In this way the charges do not create a field large enough to affect the motion of other charges in the sheet, leaving the only applied force on the sheet coming from  $E_a$  generated by the direct current (DC) voltage pulse. We define the total charge collection,  $Q_0$ , as the total charge produced by the light generating the sheet of charges. At long enough times, it is possible to collect all of  $Q_0$ . In the presence of traps, however, it might take a very long time before  $Q_0$  can be collected. Trapped charges can be freed via thermal excitations, if traps were present they could be studied by changing the temperature of the sample and noting how much time passes for charges to be freed from their traps. We define the transit time,  $t_T$ , as the average time it takes the photocharges to traverse halfway through the sample.

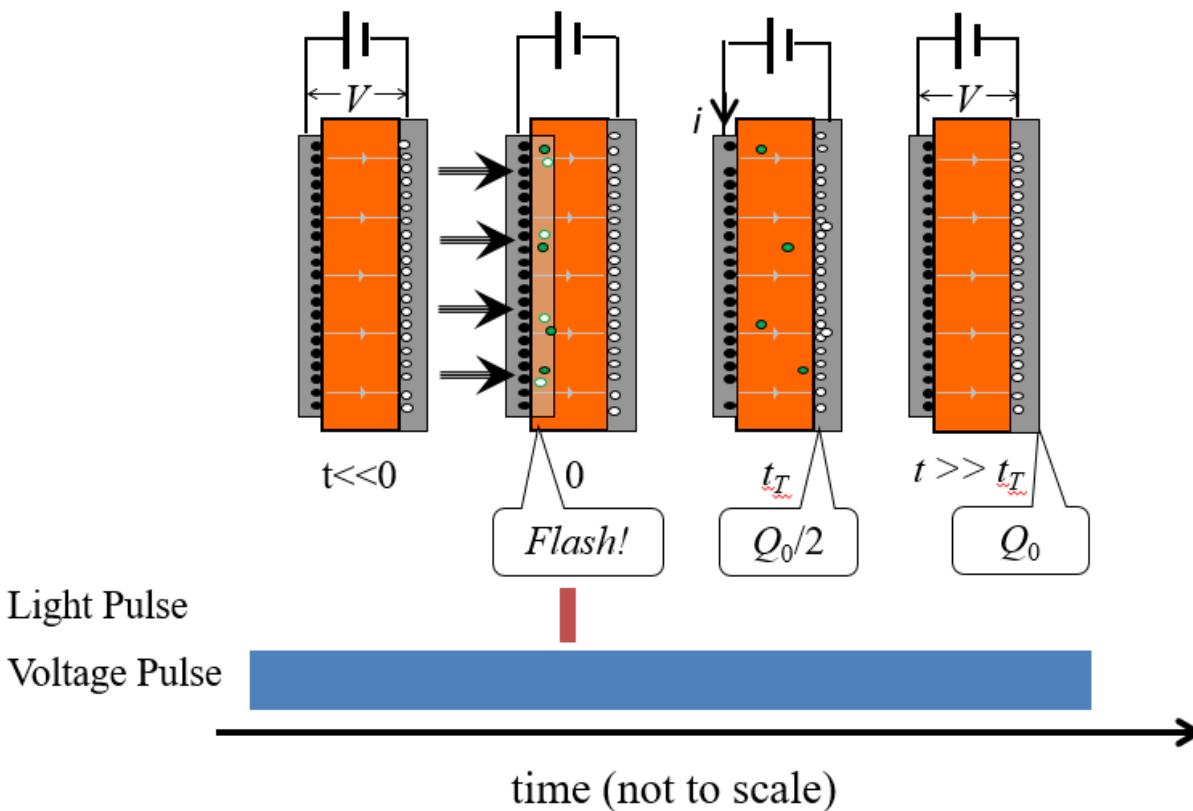


Fig. 18: Cartoon summary of the TOF process. Left, an applied DC bias,  $V_a$ , (voltage pulse) is applied which creates an applied electric field (small light arrows) through the perovskite (orange). Middle left, the light pulse (big bold arrows) generates carriers at the surface of the perovskite. Middle right, the carriers then drift due to the electric field. When half the carriers,  $Q_0/2$ , are collected we call this the transit time,  $t_T$ . Right, all carriers have been collected,  $Q_0$ , at a time much larger than the transit time.

### 2.3.1 TOF Experimental Setup

The setup for TOF is nearly identical to the dark capacitance measurement with the addition of a monochromatic light source to illuminate the front of the sample. We used a commercial 660 nm laser diode (QPhotonics, LLC., QLD-660-80S, 1 ns risetime) attached to an AVTECH AVO-9L-C pulse generator. We estimate the absorption length in the perovskite material to be about  $0.2 \times 10^{-6}$  m with 660nm light. The purpose of the laser is to synchronize a delayed pulse of light that is used to generate photocarriers. This delay is anywhere from 20-50  $\mu$ s from the initial DC voltage pulse used to instantiate a constant electric field in the perovskite in which the

generated photocharges will drift. This time delay is determined by monitoring the DC pulse voltage on the oscilloscope to ensure that the field in the sample is constant prior to photocarrier generation. For the initial set of TOF measurements, the light amplitude is adjusted such that the total photocharge is around one tenth the charge from applying a bias of 0.3 V; the mobility measurements were not noticeably affected by photocharges of this magnitude. After the amplitude of the light source has been set, it remains constant and running throughout the experiment unless otherwise noted. These measurements immediately follow from the dark capacitance measurements without changing the sample environment held under vacuum at a set temperature. In fact, the vacuum is never broken for the entire temperature dependent study for dark capacitance and TOF measurements for a given sample. A schematic of the TOF experiment can be found in Fig. 19. To eliminate the effects of small dark currents still flowing following the application of the voltage pulse about 20 microseconds before the laser pulse, we subtracted these measured currents from the measured currents following the laser pulse. The TOF analysis requires the study of strictly photocarriers traversing the sample, thus I make use of the difference between two measurements: one measurement with the light source blocked from reaching the sample (dark) and one measurement with the light source illuminating the sample (illuminated). In these types of experiments, one can assume a type of superposition between the two measurements, where illuminated data is simply dark data with photocharge effects, due to low photocarrier densities not self-interacting with the field they produce. In other words, the photocharges are small compared to the CV charge.

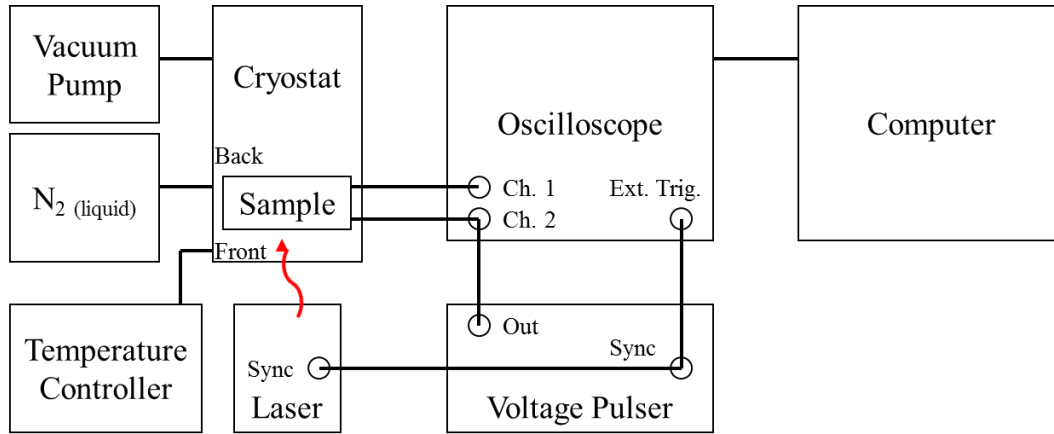


Fig. 19: Schematic of the TOF experimental setup.

### 2.3.2 Time-of-flight

In order to measure the carrier drift mobilities,  $\mu_D$ , in the cells, we use the TOF technique which measures the transient photocurrent,  $i_{photo}$ , of the photocharge carriers,  $q_{photo}$ , response due to a short pulse of monochromatic light under a constant applied bias,  $V$ . The analysis of this technique is simplified if the incident light is absorbed within a thin layer near the absorber's surface. The newly formed sheet of photocharges must then "drift" through the thickness of the absorber layer,  $d$ , until they reach the back contact. Once the photocharges arrive at the back contact, the resulting photocurrent can be measured and analyzed. Since the light pulse is very short, there are a finite amount of generated photocharges that can be extracted from the solar cell if the total electric field,  $E$ , inside the sample is large enough. When an increase in electric field produces no change in the amount of photocharge recovered, we say that the sample is complete charge collected with a total charge,  $Q_0$ . Here, photocharge is simply the integrated photocurrent.

$$q_{photo}(t) = \int_0^t i_{photo}(t') dt' \quad (2-7)$$

It is not favorable to have photocarriers generate fields which are comparable to the internal field of the cell because then an additional self-interacting term of the photocarriers would become non-negligible. Thus, a general rule is to keep the field from photocarriers, below 10% the field measured in the dark. I monitor this field by comparing the amount of the signal measured in the dark capacitance to the photo charge measured. This amounts to simply tuning the intensity of the light pulse.

### 2.3.2.1 TOF Measurement of ISU sample

In this section I will discuss the raw data findings for samples acquired from Iowa State (ISU) using the TOF description above. Samples were measured immediately after the sample thickness,  $d$ , and electronic rise time,  $t_{RC}$ , determination from the dark capacitance measurement discussed earlier without breaking vacuum. Unlike the dark capacitance measurement, the TOF measurement is done in two stages. In the first stage, a DC voltage pulse lasting 50  $\mu\text{s}$  is pulsed

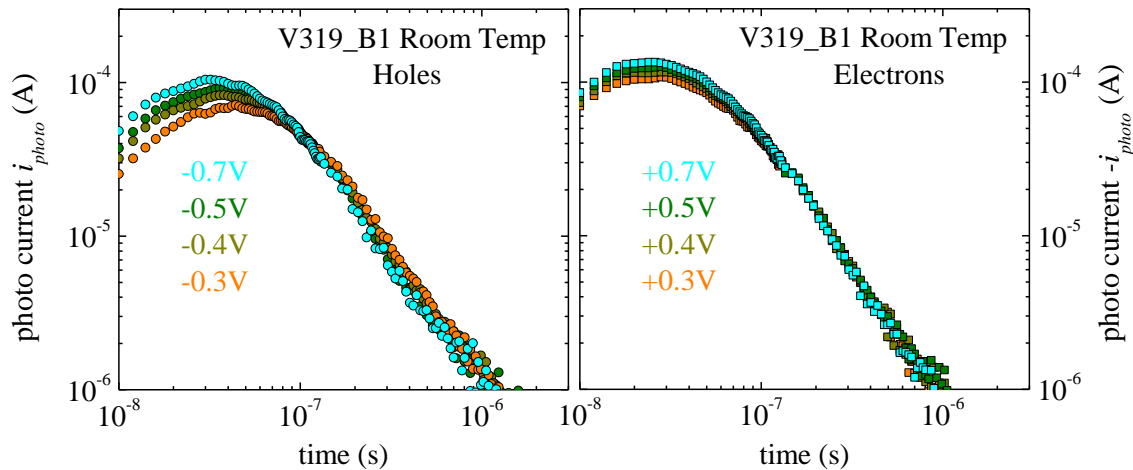


Fig. 20: Photocurrent transients (magnitude) for different applied reverse biases (left) and forward biases (right) in V319\_B1 at room temperature.

at 2 Hz. I then average over the signal for 100 cycles in the dark, which I call  $i_{dark}$ , just as in the

dark capacitance measurement. The current acquired from this stage builds up and then becomes negligible after a few microseconds, see Fig. 15. This same effect allowed us to make the dark DC capacitance measurement from before, where at long times the charge, integrated current, remained constant. The second stage exposed the sample to light from a laser diode for a duration of 5 ns (at 2Hz repetition) synchronized at a time when the dark current is negligible, usually a few microseconds after the voltage pulse is initiated. In Fig. 20, we see the resulting photocurrent from different applied voltages. We note that the photocurrent does not fall off abruptly which would represent a sheet of charges making all the way through the perovskite layer, but rather of the form  $t^{-n}$  where  $n$  is some positive real number. We also note that the later time current behavior is similar for all applied bias, that is  $n(V_a)$  is constant.

For Fig. 21 we've calculated the transient photocharges for different  $V_a$ . In the left hand plot we show the integration of the photocurrents (photocharges,  $q_{photo}$ ) and see that the rise time behavior is inherited from the slowly falling photocurrents. On the right hand plot we show collected photocharges at a time of 3  $\mu$ s after the initial charge collection at different applied bias. The use of these plots are standard in TOF measurements, they are necessary to establish that the charge eventual saturates at a value  $Q_0$  for a finite  $V_a$ . This establishes the condition of complete charge collection. Samples can break under large enough bias, so we exercised caution. It is extremely fortunate, and also to our knowledge never before observed, that both charge carriers could be measured from a single TOF measurement. One would expect that a forward biased solar cell would have large dark currents that would preclude observation of the photocharge transients.

One issue that arises from this effect is that we observe charge transients that switch from negative to positive in a single transient. This effect can be seen in Fig. 21 (left), for the  $V_a = 0$  V

transient. It cannot be interpreted using a uniform built-in field; we discuss this further in a later section. The curve through the data of the right panel involves a deep-trapping model. The idea is that carriers that are in transit for long times get captured by defects or grain boundaries before they can finish crossing the sample. As a consequence, we don't observe complete collection of these charges within the 3  $\mu\text{s}$  time window. We extracted a "deep trapping mobility lifetime product" from this behavior.

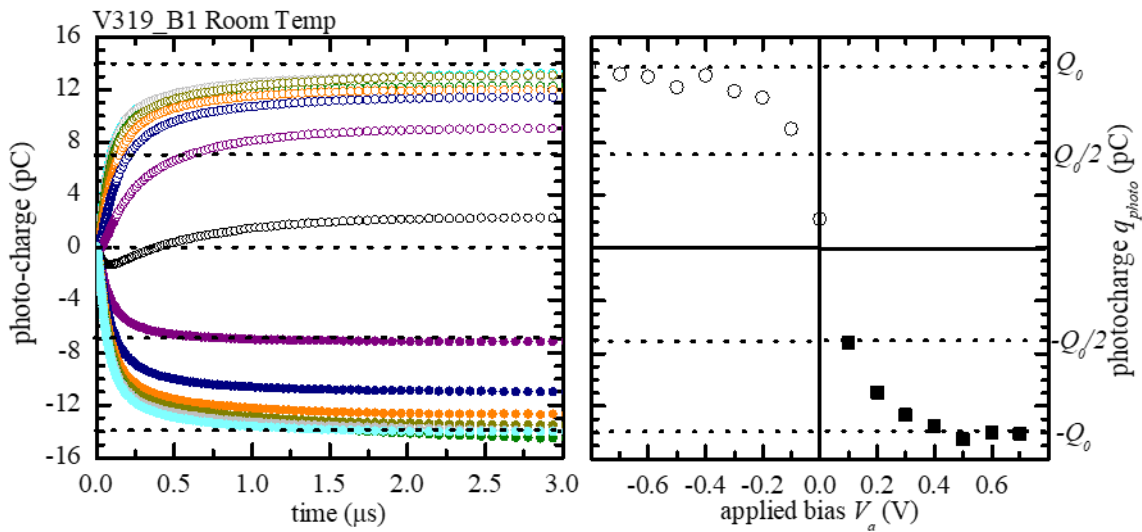


Fig. 21: (left) Photocharge transients at room temperature of sample V319\_B1 from ISU. Open circles represent transients that correspond to a net hole contribution for a given  $V_a$  and closed circles are for transients that correspond to a net electron contribution. (right) Photocharge vs. applied bias plot showing the photocharge collected at 3  $\mu\text{s}$  for different  $V_a$ . The open circles (filled squares) represent hole (electron) data where the dotted lines represent the total charge collection  $Q_0$ .



### 2.3.2.2 TOF Measurement of NREL sample

In this section I will discuss the raw data findings for samples acquired from the National Renewable Energy Laboratory (NREL) using the same method as was used with the ISU samples. In Fig. 22 we see the resulting photocurrent from eight applied voltages. As observed in

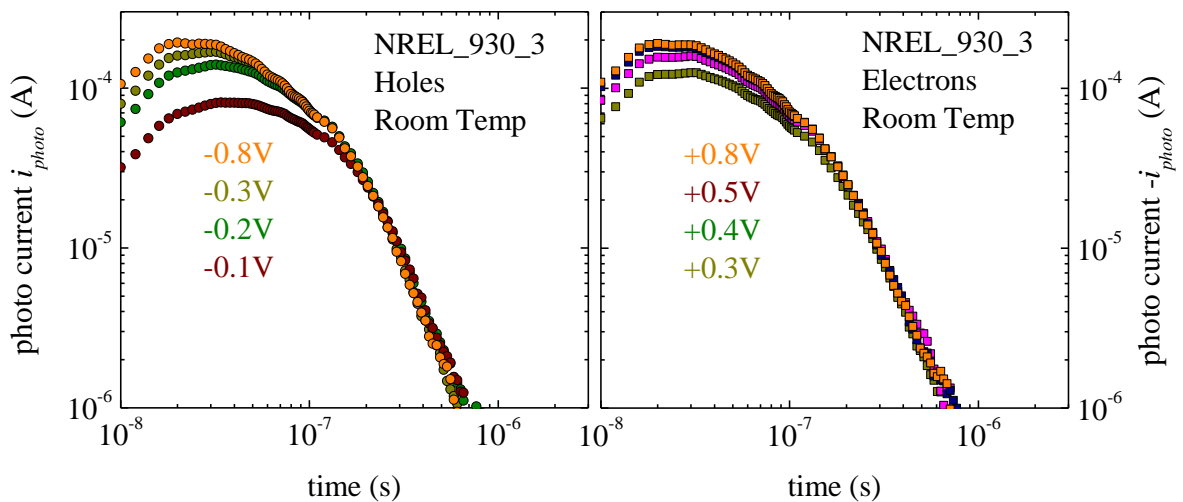


Fig. 22: Photocurrent transients for different applied reverse biases (left) and forward biases (right) in NREL\_930\_3 at room temperature.

the ISU samples, we again see that the photocurrent decreases as a power law and is constant across the entire range of biases measured. We also note that the post-transit time current behavior is similar for all applied bias.

For Fig. 23, we once again observe that the photocharges are not being collected in a normal way. We can once again observe both holes and electrons in one continuous experiment and we see that they interfere in a non-trivial way at low applied bias. Modeling these effects at low applied bias might yield some interesting physics, however, without a way to test only one carrier at a time the results would merely reflect a phenomenological approach at this time.

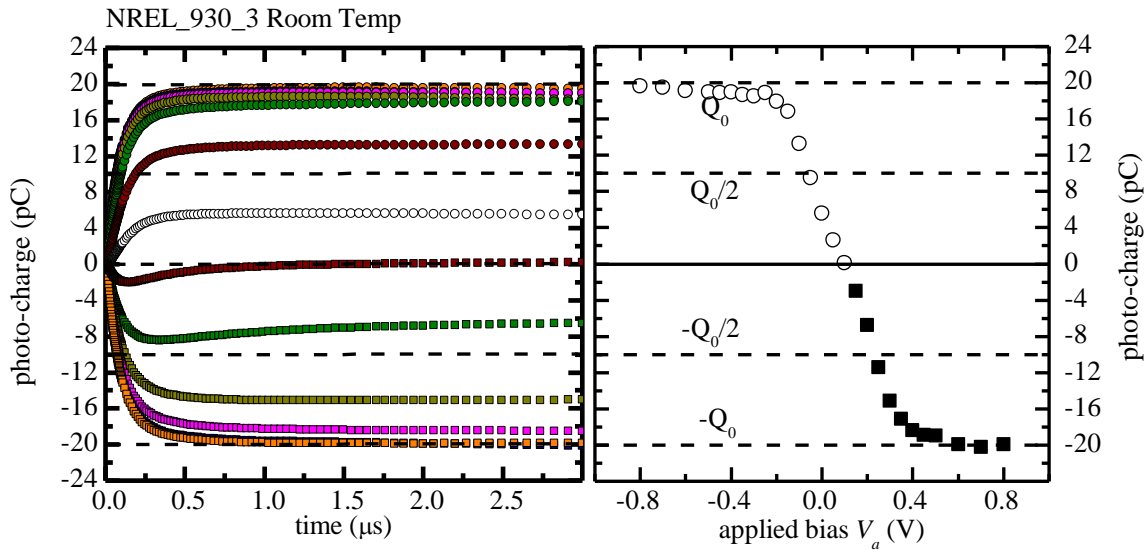


Fig. 23: (left) Photocharge transients at room temperature of NREL\_930\_3. Open circles represent transients that contribute to a net hole contribution for a given  $V_a$  and closed circles are for transients that contribute to a net electron contribution. (right) Photo-charge vs. applied bias plot shows the photocharge collected at 3  $\mu$ s for different  $V_a$ . The open circles (filled squares) represent hole (electron) data where the dotted lines represent the total charge collection  $Q_0$ .

### 2.3.3 Drift Mobility Determination (with dispersion)

For our analysis we also need to define a transit time,  $t_T$ . We use the definition that an initially narrow photocharge distribution has a mean position that is halfway across the perovskite layer thickness, which corresponds to the time it takes to collect half the total charge.

$$q_{photo}(t_T) = Q_0/2 \quad (2-8)$$

Though we have displayed this value previously, we now highlight its usefulness. We first treat the simplest case where the drift velocity  $v_D$  of the photocharge distribution is constant  $v_D = \mu_D E$ . This type of behavior is what we will refer to as “normal” transport and reflects the simplest transport model in that it is free of trap states and dispersion. In normal transport  $t_T$  is inversely

proportional to  $E$  such that  $\mu_D$  is constant, rather,  $v_D$  is proportional to  $E$ . The presence of the factor 2 in the denominator stems from how we defined  $t_T$ .

$$i_{photo}(t) = \begin{cases} Q_0/2t_T, & t < 2t_T \\ 0, & t > 2t_T \end{cases} \quad (2-9)$$

$$\mu_D = \frac{d}{2t_T E} \quad (2-10)$$

This of course is a simplistic model that neglects diffusion effects.

In the presence of normal transport with deep-trapping, i.e. when the photocarriers get trapped in defect states which have higher energies compared to the thermal energy that is available to the photocarrier, the measured drift velocity is still constant. However, the total charge collected for smaller values of  $E$  will fall short of  $Q_0$ . This will once again yields a constant  $\mu_D$ . It is not at all necessary for  $\mu_D$  to be constant in all materials. This brings us to our last transport model that we shall discuss.

Dispersive transport is a spreading of the initial "sheet" of photocarriers distribution in the direction of motion. This spreading is in addition to, and generally much larger, than the diffusive broadening of a sheet of carriers as time passes. Pioneering work on this subject, relating to modeling transport phenomena, was performed by H. Scher and E. Montroll in the 1970s.<sup>36</sup> Unlike normal transport where  $i_{photo}$  is constant, Scher and Montroll proposed that, if the transport of a charge carrier is dispersive then there should be a power law behavior between  $i_{photo}$  at  $t_T$ .

$$i_{photo}(t) = \begin{cases} i_0(t/t_T)^{-1+\alpha}, & t < t_T, \quad (pre - transit) \\ i_0(t/t_T)^{-1-\alpha}, & t > t_T, \quad (post - transit) \end{cases} \quad (2-11)$$

These expressions are consistent with the earlier definition of the transit-time as corresponding to half-collection of the total photocharge  $Q_0$ . Here  $i_0 = Q_0/(2\alpha t_T)$  and  $\alpha$  is the dispersion parameter which ranges in value from 0 to 1. Dispersion has a second implication, which is that the drift mobility (as defined above) has an implicit dependence on the actual transit time. The drift mobilities at two different transit times are related according to:

$$\mu_D(t_{T,1}) = \mu_D(t_{T,2})(t_{T,1}/t_{T,2})^{\alpha-1} \quad (2-12)$$

Dispersive transport can have several origins, including a distribution of trapping states (the “multiple-trapping” model),<sup>37</sup> spatial effects (“fractal structure”),<sup>38</sup> and some models in which carrier transport is due to hopping between localized states.<sup>39</sup>

We’ll return to mechanisms for dispersion in perovskite layers in Chapter 3. Dispersion already looks promising from our observation of the log photo-current at long times in the samples from both ISU and NREL. An equivalent result that will be useful for discussion is:

$$\mu_D = \frac{\mu_0}{\alpha} (\nu t_T)^{\alpha-1}. \quad (2-13)$$

Here we have introduced two fitting parameters, though  $\mu_0$  can be viewed as some drift mobility at a transit time  $1/\nu$ .

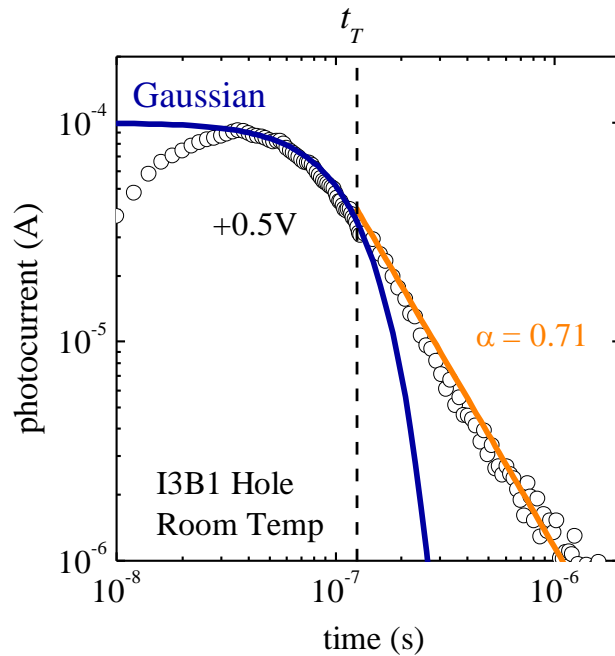


Fig. 24: Photocurrent transient for different applied reverse biases, displaying Gaussian "normal" transport, blue line, and post transit dispersive transport, orange line with  $i_0 = 44 \mu\text{A}$ ,  $t_T = 120 \text{ ns}$ , and  $\alpha = 0.71$ . For reference, a dashed vertical line marks the transit time for  $V_a = -0.5 \text{ V}$ .

As can be seen from Fig. 24, the Gaussian appears to fit well for pre-transit times whereas the dispersive model fits better for post transit times. It is important to remember that the RC time is around 70 ns in this sample and plagues the analysis of the pre-transit photocurrent. There is a delicate balance in our data between the RC time constant and when the photo-current signal is low and becomes noisy. It is for this reason that we look at the behavior of the integrated photo-current (photo-charge). It is important to note that all of the dispersion parameters were calculated from post transit decays, see Fig. 24, were not how the dispersion parameters were measured. The analysis of all transit times at varying applied biases were compared at a specific temperature to get an average dispersion parameter, see Fig. 27. The value of dispersion from post transit decays does not vary far from the average dispersion value.

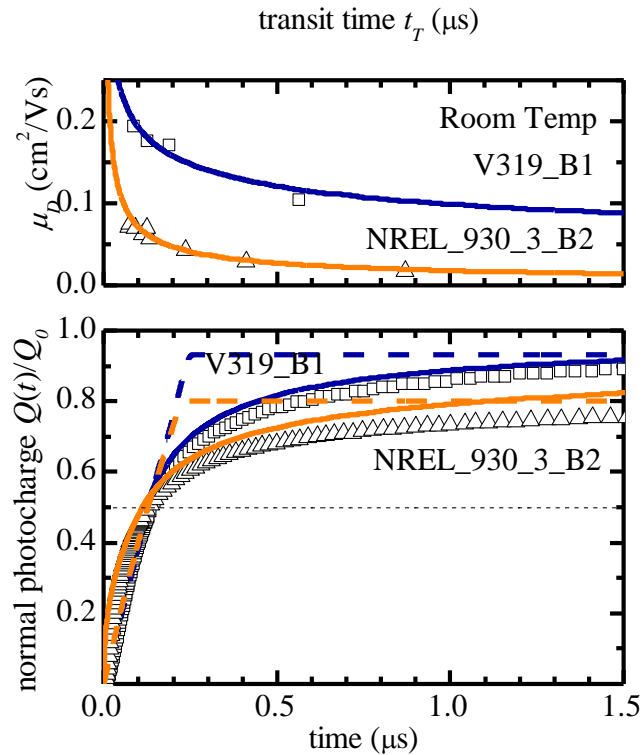


Fig. 25: (top) The symbols illustrate drift-mobilities as a function of transit times for two samples. The solid lines are fits to these data given dispersion parameters of 0.71 (ISU V319\_B1) and 0.40 (NREL\_930\_3\_B2); see equation xx. (bottom) The symbols indicate normalized photocharge transients for two samples; the transients were chosen to have transit times close to 130 ns; by definition, the charge transients pass the value 0.5 at the transit time. The solid lines indicate dispersive transport calculations using the same dispersion parameters used for the top panel. The dashed lines are calculations using normal transport with deep-trapping.

In the top part of Fig. 25 we see a summary of the drift mobilities found from the samples at room temperature. The dispersion model is used to fit the mobilities with Eq. 2-13. At this time I would like to remind the reader that drift mobilities calculated in samples with dispersion

are transit time dependent. That is for highly dispersive samples, low  $\alpha$ , the initial sheet of photo-charge spreads, or “disperses”, faster than a sample that is less dispersive, higher  $\alpha$ .

On the bottom portion of the figure we show the best fits for the photocharge transients selected to both have transit times of 130 ns. In this case it is quite clear that the dispersive model fits the data quite well. It is remarkable that the dispersion model does not require information on the applied bias, rather, just the transit time and dispersion parameter. For reference, the dashed lines that indicate normal transport including deep trapping. In this model the photocarriers traverse the sample as a thin sheet with some of the carriers being caught in trap states (thus not experiencing full charge collection). This comparison is made to rule out the normal deep trapping scenario.

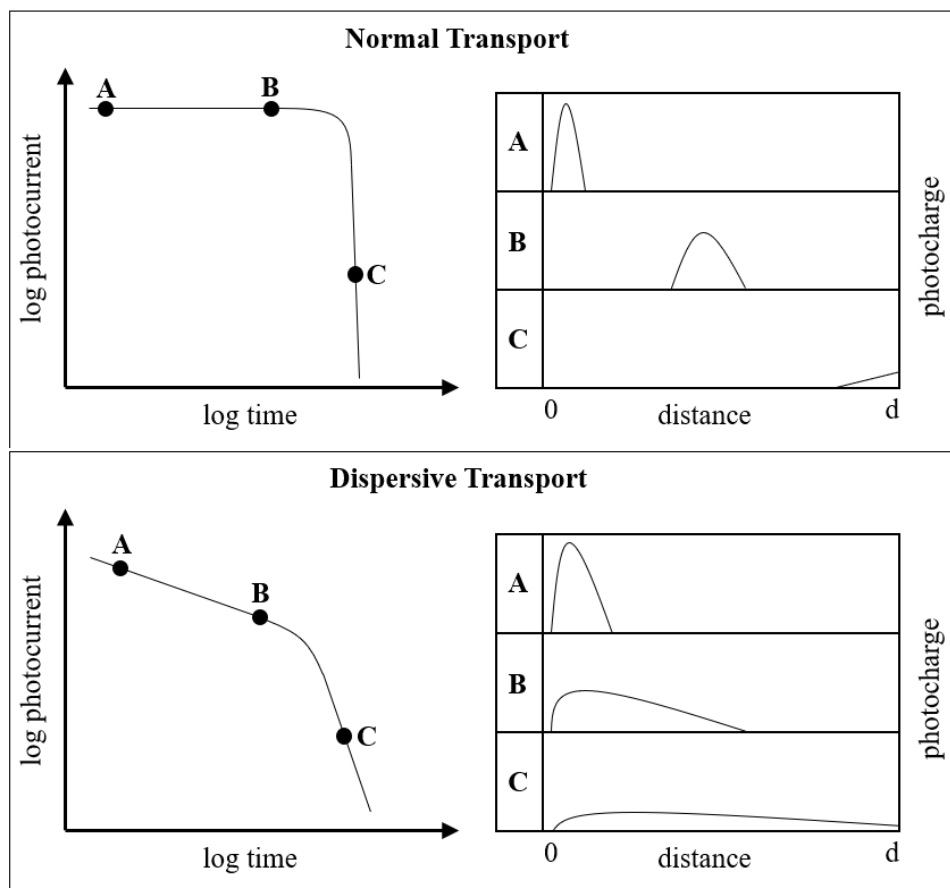


Fig. 5: Cartoon of photocurrents and photocharge distributions of normal (top) and highly dispersive, low  $\alpha$ , transport (bottom).

I have included Fig. 5 from the previous chapter, for convenience, to act as a visual guide to understand the phenomenology of dispersive transport. The diagram is not at all to scale, though the area under the distributions at each time step are meant to be equal and represent the total charge,  $Q_0$ . The middle plot shows some spreading of the sheet and the last plot shows our definition of transit time, when half of the total charge traverses the sample. A quick remark on the justification of our choice shows that the transit time measures the average velocity of the entire distribution. This model also gives us insight on why the post-transit current fades much slower than in our other models.



### 2.3.4 Temperature Dependence

I would finally like to discuss the temperature dependence of the drift mobilities and dispersion parameters of the samples. I measured the samples in the setup described above in the discussion on dark capacitance and TOF, see schematic in Fig. 19. I used thermal grease to couple my sample thermally to the cryostat. Measurements were initially made at room temperature. Afterwards, the sample temperature was increased to the high range of 325K. After measurements were made, the temperature was reduced and the process was repeated at cooler and cooler temperatures until around 175K. Each temperature dependent study was performed over the course of two days.

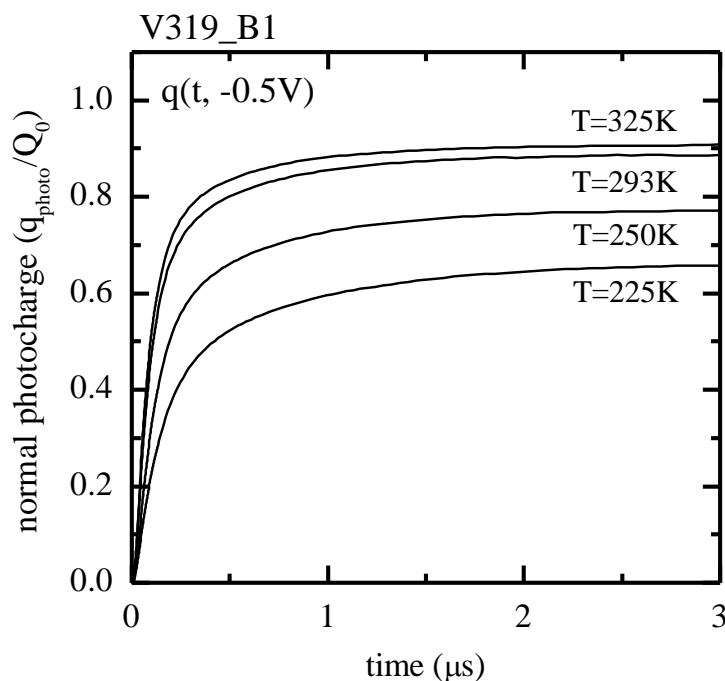


Fig. 26: Temperature dependence of charge transients (normalized to  $Q_0$ ) at an applied bias of -0.5 V.

In Fig. 26 the normalized photocharge transients are shown for four different temperatures. As is evident, the “transit time” gets much longer as the temperature falls. The

lessening of photocharge at lower temperatures corresponds to a decrease in the hole drift mobility that we'll show in more detail shortly.

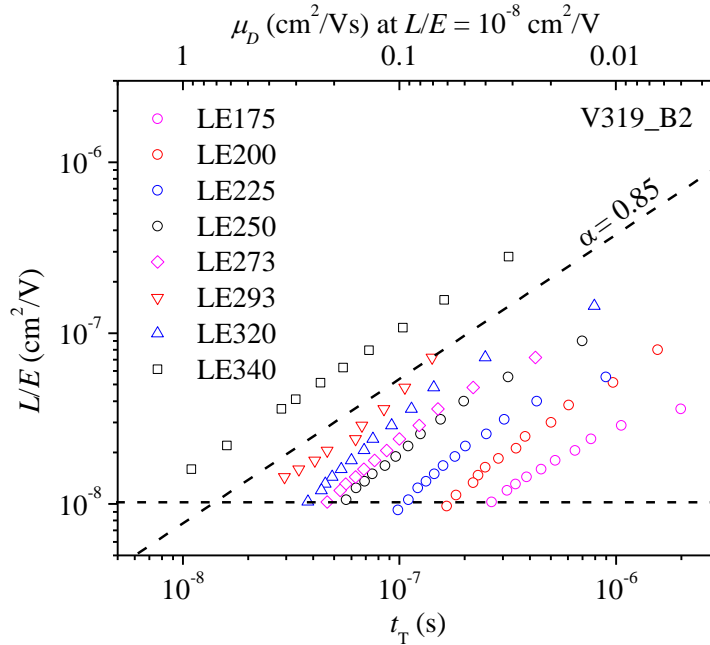


Fig. 27:  $L/E$  vs. transit time plot of holes for a range of temperatures in V319\_B2.

In Fig. 27 we see how the quantity  $L/E$  varies with the transit time. Here we define  $L/E$  as the distance a charge travels per given electric field:

$$\frac{L}{E} = \frac{d^2}{2(V-V_0)} \quad (2-14)$$

Since we have defined the transit time above as the time when half the total charge is collected, we can define,  $L = d/2$ , as the average displacement of the charge carriers during the transit time.  $V_0$  is the correction to the internal field obtained from the cross over observed from the photocharge vs. applied bias plot, see right side of Fig. 21 and Fig. 23. For our samples  $V_0$  is a small correction rarely more than 10% of the field at low applied bias.

There are a few interesting things with the behavior of  $L/E$  that I would like to discuss before moving on. First,  $L/E$  has dimensions of a mobility lifetime product. That is to say, that

$$\mu_D t_T = \frac{L}{E}. \quad (2-15)$$

Even more interesting is that any similar increase in both  $L$  and the field  $E$  would cancel and have no effect on the mobility lifetime product.

## 2.4 Summary

We received samples from ISU and NREL to measure the drift mobility. Perovskite samples degrade quickly and the opportunity to go back and remeasure samples was not feasible for longer experiments such as temperature dependent TOF measurements. Samples arrived on a glass superstrate, each with around four or more contact points for measurement. These contacts started off too large and samples too thin which yielded electronic rise times greater than transit times,  $t_{RC} > t_T$ . These early samples were carefully scribed to reduce the area of the contact, thus reducing the capacitance, in hopes of finding a signal. It is important to note that the drift mobility relates to the transit time in TOF measurements, and at this point the mobility was unknown. It was fortunate that we were able to get a signal with our scribing method and thus an order of magnitude estimate of the mobility. Samples from then on were sent with smaller contacts and thicker perovskite layers so that accurate measurements could be performed reducing the electronic rise time from  $\sim 10^{-6}$  s to  $\sim 10^{-8}$  s.

After the rise time for the sample dot was established, we would measure the drift mobility using the TOF method. We observed early on that samples had photocurrent behavior atypical of normal transport, having power law post transit decays. A fortunate surprise was finding that the

samples allowed for determination of both charge carriers mobility without the need to break vacuum or special contacts.

I also discovered that the cells measured were found to be dispersive. To reiterate, to be dispersive means that the drift mobility is dependent on the time it takes photocharges to traverse the sample.

Lastly, I found that the dispersion parameter,  $\alpha$ , is independent, or weakly dependent, on temperature. This is not the first time such a behavior has been observed,<sup>40</sup> and may hint at something like partially aligned ferroelectric domains inside the perovskite.<sup>41</sup> A summary of our results can be found in Fig. 28. I have included an extra table that summarizes sample information at room temperature, see Table 2.

Sample	Thickness $\mu\text{m}$	$V_{OC}$ V	$\mu_h$ $\text{cm}^2/\text{Vs}$	$\alpha_h$	$\mu_e$ $\text{cm}^2/\text{Vs}$	$\alpha_e$
I3B1	1.20	0.62	0.21	0.71	1.4	0.56
I3B2	1.20	0.65	0.53	0.84	-	-
N3C3	0.80	0.90	0.14	-	0.72	-
N4C3	0.89	1.00	0.063	0.40	0.11	0.43

Table 2: Sample codes - I: Iowa State University; N: National Renewable Energy Laboratory. Mobilities and dispersion parameters correspond to the displacement-field ratio  $L/E = 10^{-8} \text{ cm}^2/\text{V}$ .

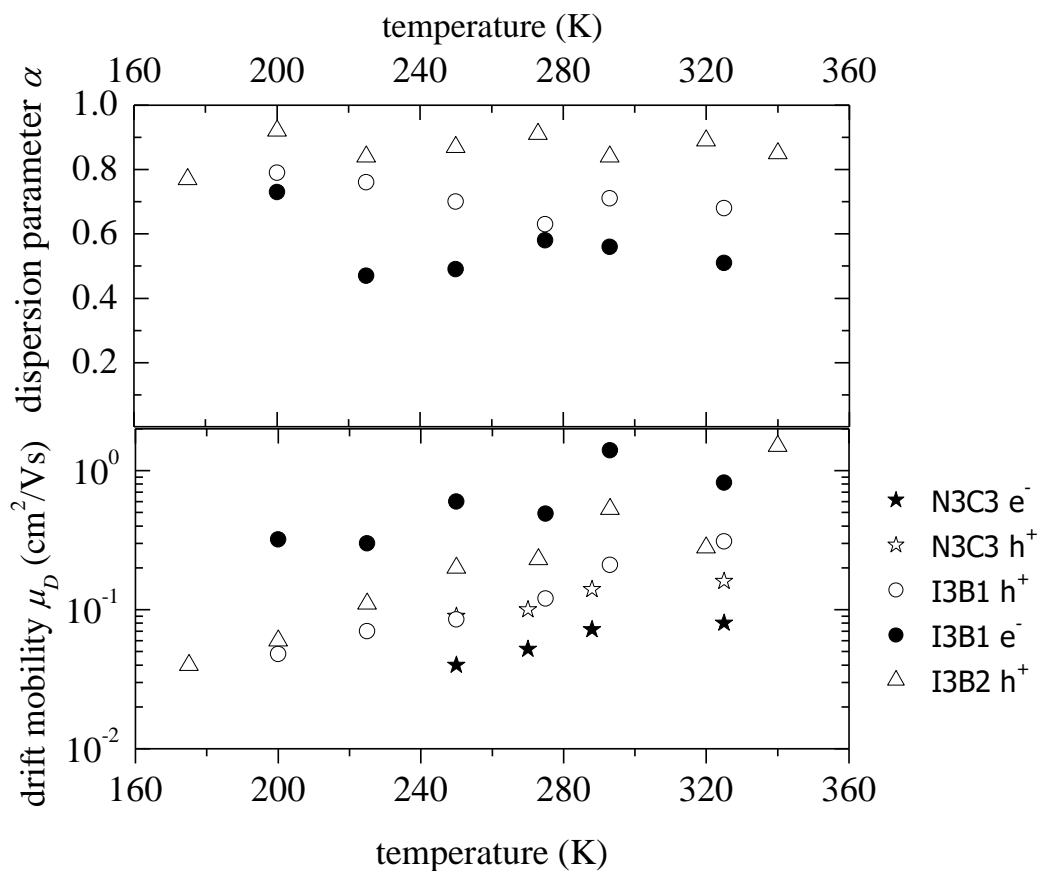


Fig. 28: Summary of temperature dependence of dispersion parameter (top) and drift mobility (bottom) for various samples. The drift mobilities correspond to  $L/E = 1.0 \times 10^{-8} \text{ cm}^2/\text{V}$ . Open triangles represent hole data from V319\_B2, open (closed) circles represent hole (electron) data from V319\_B1, and open (closed) stars represent hole (electron) data from NREL3\_C3.

### 3. Discussion and Physics Implications

In the previous section we discussed the photocarrier time-of-flight (TOF) measurement for methyl-ammonium lead iodide, perovskite structured, solar cells. In particular we found that this material has a transit-time dependent drift mobility,  $\mu_D(t_T)$ . Due to this dependence, the material is called dispersive with a dispersion constant  $\alpha$ . Even more surprising we found that the dispersion parameter is, at most, weakly dependent on temperature. Care is needed to compare other measurements because of this time dependence and our choice of  $L/E$  value. In the first section we shall discuss different types of measurements used to obtain a drift mobility. A summary of mobilities made with different techniques is given in Table 3.

<i>Mobility Measurement</i>	<i>Time of Flight</i>	<i>DC Space-Charge Limited Currents</i>	<i>THz Spectroscopy</i>	<i>Hall Effect</i>
$\mu$ (cm <sup>2</sup> /Vs)	1(e) 0.2(h) <sup>(42)</sup>	2.5 <sup>(43)</sup>	12.5(e) 7.5(h) <sup>(44)</sup> 8 <sup>(45)</sup>	1.5 <sup>(46)</sup> 66 <sup>(47)</sup>
type	thin film	single crystal	single crystal / scaffold Al <sub>2</sub> O <sub>3</sub>	thin film / single crystal
non-dispersive	great	ok	great	assumes effective mass
dispersive	great	transient only, difficult	no fundamental theory, difficult	no fundamental theory
device applicability	ok	ok	not in a relevant time domain	not quantitative

Table 3: Comparison of different measurements for their ability to measure mobilities for dispersive and non-dispersive materials.

### 3.1: Hall Effect Measurement

The Hall effect<sup>48</sup> is the oldest way to measure the charge carrier mobility of a material. This effect is related to the Lorentz force acting on the effective mass,  $m_{eff}$ , of the moving charge with acceleration  $\mathbf{a}$ :  $m_{eff}\mathbf{a} = q\mathbf{v} \times \mathbf{B}$ .

The electrical current through the sample defines the direction of the drift velocity  $\mathbf{v}$ , and the magnetic field  $\mathbf{B}$  is aligned normal to the current and to a surface of the sample. Charge then builds up to create an induced voltage across the material called the Hall voltage,  $V_H$ . Based on the strength of the current and magnetic field one can deduce the Hall resistance,  $R_H$ , of the carriers inside the material. We can then relate the Hall resistance to the density of carriers,  $n$ , with charge  $e$ . This result is summarized in Eq. 3-1.

$$R_H = -\frac{1}{ne} \quad (3-1)$$

Assuming the material is well ordered, we can relate the mobility to this value by Eq.3-2,

$$\mu_H = -R_H\sigma, \quad (3-2)$$

where  $\sigma$  represents the conductivity of the material.

We distinguish between Hall mobility,  $\mu_H$ , and drift mobility,  $\mu_D$ , in the sense that there is some ambiguity using the Hall effect. The reason for this issue arises because of an ill-defined band structure near the band edge, which is certainly the case for a disordered material like amorphous Si, for which the Hall Effect does not even correctly identify the majority carrier.<sup>49</sup> Drift mobilities determined from the Hall effect are derived using the Drude model. In the case of disordered materials, more exotic theories, i.e. “hopping” models, may be applied to explain the data. However, this measurement works particularly well with highly ordered crystals, especially alkali metals and crystalline semiconductors, in which the DC conductivity is well modeled by

Drude.<sup>50</sup> Using the Hall effect to understand the transport behavior is also worrisome in many disordered materials due to the failure to predict time dependent effects, such as dispersion.

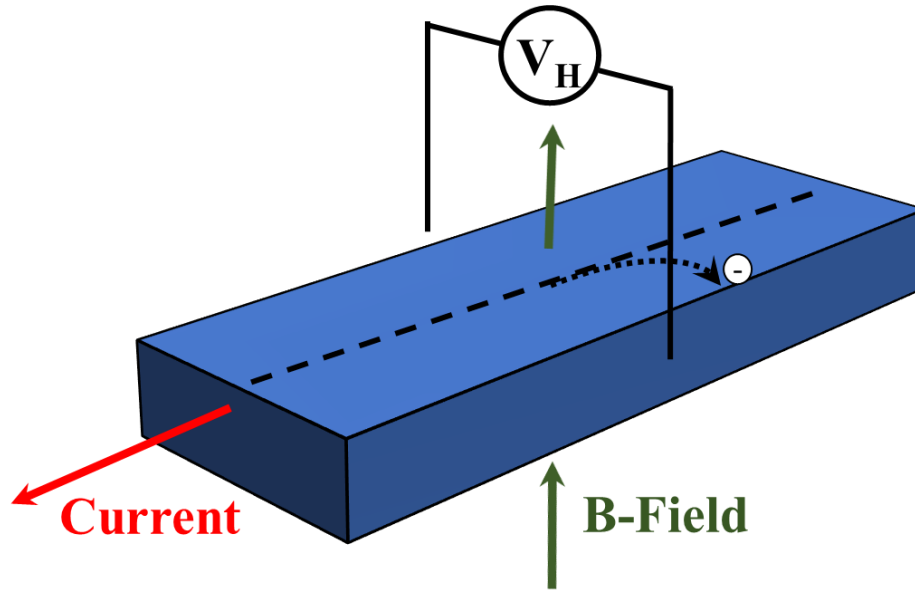


Fig. 29: Schematic of DC Hall measurement.

### 3.2: THz Photoconductivity Measurement

The THz measurement utilizes THz frequency resolution, which corresponds to picosecond ( $10^{-12}$  s) time domain. This method works by taking picosecond resolution snapshots of a waveform that are separated by a small delay-time step. These snapshots give information about the conductivity,  $\sigma$ , of the material and can be related to the total mobility,  $\mu_e + \mu_h$ , multiplied by the charge generation quantum yield,  $\xi$ , see Eq. 3-3.<sup>27</sup>

$$\Delta\sigma = \xi(\mu_e + \mu_h) = -\frac{\Delta E_{exc}(\omega)\epsilon_0 c}{\Delta E_{gs}(\omega)F e_0} \frac{1}{1-e^{-\alpha L}} \quad (3-3)$$



The measurement requires information on the ground state of the THz wave's electric field,  $\Delta E_{\text{gs}}$ , the fluence of photons from the excitation light (light being absorbed by the material),  $F$ , the absorption coefficient,  $\alpha$ , at the excitation wavelength,  $\omega$ , and the thickness of the material,  $L$ . The constants:  $\epsilon_0$ ,  $e_0$ , and  $c$ , represent the electric permittivity of free space, the fundamental charge of an electron, and the speed of light, respectively. The excited state of the electric field captured by the THz wave,  $\Delta E_{\text{exc}}$ , is measured by the detector only after photoexcitation has created a sheet of charges inside the material and represents the electric field induced by photoexcitation. Whereas  $\Delta E_{\text{gs}}$  is obtained by firing a THz wave through the sample prior to photoexcitation (a THz probe of the electric field inside the material in the dark). The relation of the conductivity to the mobility is derived with the Drude model which assumes the material is a pure crystal. Since the measurement is performed in the picosecond time domain, we are far outside the operating conditions of real solar cell devices.

The measured values of the mobilities from Ponseca et al.<sup>27</sup> and Wehrenfennig et al.<sup>28</sup> are of order  $10 \text{ cm}^2/\text{Vs}$  and  $8 \text{ cm}^2/\text{Vs}$  respectively, see Table 2. These values, considering a  $\sim 10^{-12} \text{ s}$  time domain, yields surprising consistent results with our samples with dispersion. In Ponseca's measurement they used a sample with thickness 200 nm and measured a mobility of  $12.5 \text{ cm}^2/\text{Vs}$  for electrons at room temperature. If we assume that their sample is comparatively dispersive to what was studied in this dissertation, i.e.  $\alpha = 0.7$ , we can compare their mobility to our quoted values at an  $L/E = 10^{-8} \text{ cm}^2/\text{V}$ . We find, surprisingly, that  $\mu_{\text{D}}(10^{-8} \text{ cm}^2/\text{V})_{\text{THz}} = 0.63 \text{ cm}^2/\text{Vs}$  which is consistent with our measured values. Wehrenfennig's measurement is similarly consistent.

Wehrenfennig<sup>51</sup> shows transient photoinduced response for different fluences. This measurement should be sensitive to dispersion effects at low fluences (where Langevin and Auger recombination effects are negligible) and should show up as a decay in the signal. It is curious that the MAPbI<sub>3</sub> plot tucked away in the Supplementary Materials does exhibit slight visible variation of the photoinduced response between a few picoseconds to two nanoseconds. It may also be the case that Langevin recombination is still dominating the decay at the induced charge density. This effect is less clear for the main article's plot displaying signals from MAPbI<sub>3</sub> (3:1) and MAPbI<sub>3-x</sub>Cl<sub>x</sub>.

### 3.3: Space Charge Limited Currents

Space charge limited currents (SCLC) are an interesting way to extract a mobility from a material as well. When a relatively modest bias is applied to a material, the current-voltage characteristic will be linear, and we call this region "Ohmic" after Ohm's Law which describes its behavior. However, Ohm's Law breaks down if space charge builds up sufficiently in the bulk of the sample causing an injection of charge carriers from the contacts. In the simplest case the current scales as the square of the applied bias voltage. This relation is better known as the Mott-Gurney law<sup>52</sup>:

$$J = \frac{9}{8} \frac{\varepsilon \mu V_A^2}{d^3} \quad (3-4)$$

where  $J$  is the current density,  $\varepsilon$  is the permittivity,  $\mu$  is the drift mobility of the charge carriers,  $V_A$  is the applied bias, and  $d$  is the distance between the two electrode contacts. With *a priori* knowledge of the permittivity and distance, one can simply fit a current voltage measurement on a log-log scale with the resistance as a fitting parameter for the bias domain where the current is Ohmic and the mobility as a fitting parameter in the SCLC region.

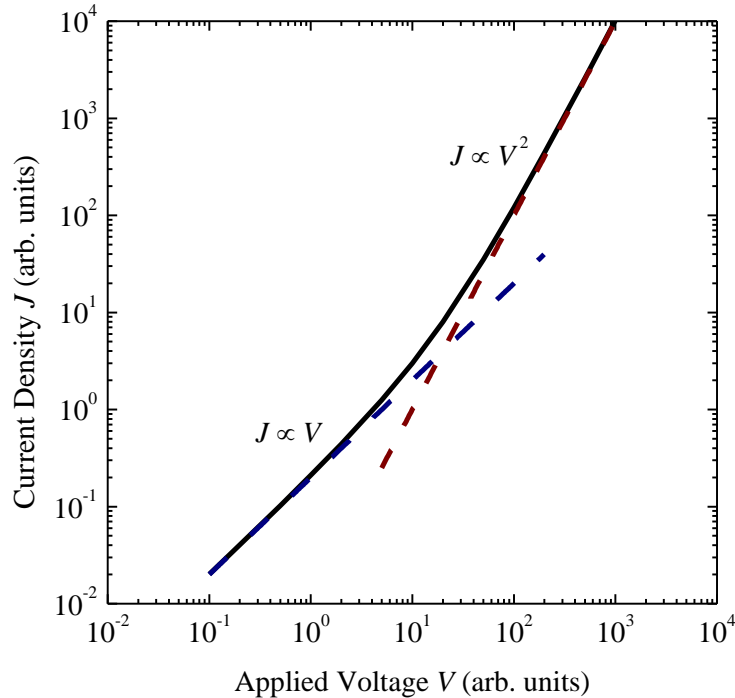


Fig. 30: Illustration of  $J$ - $V$  relation of material exhibiting SCLCs without traps. The lower voltage region is modeled by a linear (Ohm's Law) relationship, whereas the higher voltage region exhibits a power law relation of order two.

Shi et al. made SCLC measurements on a single crystal of size 1.64mm x 2.76mm x 2.76mm.<sup>53</sup>

They found that the mobility of their crystals of  $\text{CH}_3\text{NH}_2\text{PbI}_3$  was around  $1 \text{ cm}^2/\text{Vs}$ . The value that they measured is slightly higher than the value we report and does not appear to be dispersive (i.e. the sample has a constant mobility for increasing field inside the sample). Though without a transient measurement we cannot say conclusively how this differs due to our drift mobility being transit time dependent. This is not discouraging because they used single crystal perovskite for their measurement and dispersive behavior seems only to happen in materials with disorder; however, puzzling how a perfect crystal can have such a low mobility, see Table 2. The results are actually hard to compare without a transient study of the field dependence. Also remember that our choice of  $L/E$  field to quote the mobility value at ( $10^{-8} \text{ cm}^2/\text{V}$ ) was chosen to

resemble operating conditions of a working solar cell device though on physical grounds this value is arbitrary. For comparison, dispersive porous Si reported values of mobility at an  $L/E$  field of  $1.6 \cdot 10^{-10} \text{ cm}^2/\text{V}$ .<sup>54</sup>

### 3.4: A Final Note on Perovskites

Perovskites studied in this dissertation have solely focused on thin film  $\text{CH}_3\text{NH}_3\text{PbI}_3$  ( $\text{MAPbI}_3$ ) and mobilities were found to be modest with conditions resembling device operation,  $10^{-1} \text{ cm}^2/\text{Vs}$ . There are other perovskite materials that have shown larger mobilities than  $\text{CH}_3\text{NH}_3\text{PbI}_3$ . Below is a table for some values.

Measurement	Single Crystal Perovskite and $\mu$ ( $\text{cm}^2/\text{Vs}$ )			
Hall Effect <sup>25</sup> (Stoumpos)	$\text{MAPbI}_3$ 66	$\text{MASnI}_3$ 2320	$\text{MA}_3\text{Sn}_{0.5}\text{Pb}_{0.5}\text{I}_3$ 270	$\text{CsSnI}_3$ 103
Hall Effect <sup>24</sup> (Chen)	$\text{MAPbI}_3$ 11	$\text{MAPbBr}_3$ 60		
SCLC <sup>26</sup> (Shi)	$\text{MAPbI}_3$ 2.5	$\text{MAPbBr}_3$ 38		

Table 4: Comparison of different mobilities measured from groups who studied multiple perovskite compounds.

Of the perovskites used for solar cell device research,  $\text{MAPbI}_3$  has certainly acted as the catalyst for recent improvements in perovskite type cells in the past decade. Due to the stability issues that plague  $\text{MAPbI}_3$ ,<sup>55,56,57,58</sup> many groups have chosen to study other types of perovskites that might someday be competitive with silicon. The current world record efficiency for perovskite solar cells is 22.7%, held by KRICT<sup>59,60</sup> using formamidinium lead iodide,  $\text{NH}_2\text{CHNH}_2\text{PbI}_3$  or

FAPbI<sub>3</sub>. Though for MAPbI<sub>3</sub> the highest efficiency seen is ~19.5%.<sup>61</sup> For comparison, single crystal silicon solar cells have reached 27.6%.<sup>62</sup>

It has been an exciting time for perovskite materials, and it seems the progress in the field will only continue to grow. Perovskite structured materials have been interesting in fields such as high temperature superconductors for quite some time now, but only within the last decade did they appear fascinating for solar cells as well. The rapid progress is due mostly to understanding transport properties of these materials. The rest of the progress is owed to the application of decades worth of research on other types of solar cells. Discovering the spatially dispersive nature of MAPbI<sub>3</sub> should help future researchers understand transport in similar materials.

## References

---

- <sup>1</sup> NREL Best Research-Cell Efficiencies. Rev April 25<sup>th</sup>, (2018).
- <sup>2</sup> Megaw H. "Crystal Structure of Barium Titanate". *Nature* **155** 3928, 484-485 (1945).
- <sup>3</sup> Hazen R, Finger L, Angel R, Prewitt C, Ross N, Mao H, Hadidiacos C, Hor P, Meng R, and Chu C. "Crystallographic description of phases in the Y-Ba-Cu-O superconductor". *Physical Review B* **35** 13, 7238–7241 (1987).
- <sup>4</sup> Stranks S. D and Snaith H. J. "Metal-halide perovskites for photovoltaic and light-emitting devices". *Nat. Nanotechnol.* **10**, 391–402 (2015).
- <sup>5</sup> Pang S, Hu H, Zhang J, Lv S, Yu Y, Wei F, Qin T, Xu H, Liu Z, and Cui G. "NH<sub>2</sub>CH=NH<sub>2</sub>PbI<sub>3</sub>: An Alternative Organolead Iodide Perovskite Sensitizer for Mesoscopic Solar Cells". *Chem. Mater.* **26**, 1485–1491 (2014).
- <sup>6</sup> O'Regan B and Grätzel M. "A low-cost, high-efficiency solar cell based on dye-sensitized colloidal TiO<sub>2</sub> films". *Nature* **353** 6346, 737–40 (1991).
- <sup>7</sup> Kopidakis N, Schiff E. A, Park N.-G, van de Lagemaat J, and Frank A. J. "Ambipolar Diffusion of Photocarriers in Electrolyte-Filled, Nanoporous TiO<sub>2</sub>". *J. Phys. Chem. B.* **104**(16):3920-3936 (2000).
- <sup>8</sup> Kojima A, Teshima K, Shirai Y, and Miyasaka T. "Organometal halide perovskites as visible-light sensitizers for photovoltaic cells". *J. Am. Chem. Soc.* **131**(17):6050–6051 (2009).
- <sup>9</sup> Kim H.-S, Lee C.-R, Im J.-H, Lee K.-B, Moehl T, Marchioro A, Moon S.-J, Humphry-Baker R, Yum J.-H, Moser J.E, Grätzel M, and Park N.-G. "Lead iodide perovskite sensitized all-solid-state submicron thin film mesoscopic solar cell with efficiency exceeding 9%". *Sci. Rep.* **2**, 591 (2012).

- 
- <sup>10</sup> Lee M, Teuscher J, Miyasaka T, Nurakami T, Snaith H. “Efficient Hybrid Solar Cells Based on Meso-Superstructured Organometal Halide Perovskites”. *Science* **338**: 643-647 (2012).
- <sup>11</sup> NREL Best Research-Cell Efficiencies. Rev April 25<sup>th</sup>, (2018).
- <sup>12</sup> Green M. A, Hishikawa Y, Dunlop E. D, Levi D. H, Hohl-Ebinger J, and Ho-Baillie A. W.Y. “Solar cell efficiency tables (version 52)”. *Prog. Photovolt Res. Appl.* **26** 427-436 (2018).
- <sup>13</sup> Yang WS, Noh JH, Jeon NJ, Kim Y.C, Ryu S, Seo J, and Seok S. I. “High-performance photovoltaic perovskite layers fabricated through intramolecular exchange”. *Science*. **348** (6240): 1234-1237 (2015).
- <sup>14</sup> Snaith H.J, Abate A, Ball J.M, Eperon G.E, Leijtens T, Noel N.K, Stranks S.D, Wang J.T.-W, Wojciechowski K, and Zhang W. “Anomalous Hysteresis in Perovskite Solar Cells”. *J. Phys. Chem. Lett.* **5**(9) 1511-1515 (2014).
- <sup>15</sup> Hoke E. T, Unger E. L, Vandewal K, and McGehee M. D. Charge recombination and transport in hybrid perovskite solar cells: why do perovskite solar cells have large Voc? in *Proc. MRS Fall Meeting and Exhibit* (2013).
- <sup>16</sup> Snaith H. J, Abate A, Ball J.M, Eperon G.E, Leijtens T, Noel N.K, Stranks S.D, Wang J.T.-W, Wojciechowski K, and Zhang W. “Anomalous hysteresis in perovskite solar cells”. *J. Phys. Chem. Lett.* **5**, 1511–1515 (2014).
- <sup>17</sup> Schiff E.A. *Sol. Energy Mater. Sol. Cells* **78**, 567–595 (2003).
- <sup>18</sup> Chen Y., Yi H. T. & Podzorov, V. High resolution *ac* measurements of the Hall effect in organic field-effect transistors, *Phys. Rev. Applied* **5**, 034008 (2016).
- <sup>19</sup> Chen Y, Yi H.T, Wu X, Haroldson R, Gartstein Y.N, Rodionov Y.I, Tikhonov K.S, Zakhidov A, Zhu X.-Y, and Podzorov V. Extended carrier lifetimes and diffusion in hybrid perovskites

---

revealed by Hall effect and photoconductivity measurements, *Nat. Commun.* 7:12253 doi:

10.1038/ncomms12253 (2016).

<sup>20</sup> Zallen R. The Physics of Amorphous Solids. Wiley-VCH. 282-289 (1983).

<sup>21</sup> Scher H. and Montroll E.W. “Anomalous transit-time dispersion in amorphous solids”. *Phys. Rev. B.* **12**, 2455 (1975).

<sup>22</sup> Spear W.E. “Transit Time Measurements of Charge Carriers in Amorphous Selenium Films”. *Proc. Phys. Soc. B* **70** 7, 669 (1957).

<sup>23</sup> Rao P.N, Schiff E.A, Tsybeskov L, Fauchet P. “Photocarrier drift-mobility measurements and electron localization in nanoporous silicon”. *Chem. Phys.* **284** 129–138 (2002).

<sup>24</sup> Chen Y, Yi H.T, Wu X, Haroldson R, Gartstein Y.N, Rodionov Y.I, Tikhonov K.S, Zakhidov A, Zhu X.-Y, and Podzorov V. “Extended carrier lifetimes and diffusion in hybrid perovskites revealed by Hall effect and photoconductivity measurements”. *Nat. Comm.* 7:12253 DOI: 10.1038. (2016).

<sup>25</sup> Stoumpos C.C, Malliakas C.D, Kanatzidis M.G. “Semiconducting Tin and Lead Iodide Perovskites with Organic Cations: Phase Transitions, High Mobilities, and Near-Infrared Photoluminescent Properties”. *Inorg. Chem.* **52**, 9019-9038 (2013).

<sup>26</sup> Shi D, Adinolfi V, Comin R, Yuan M, Alarousu E, Buin A, Chen Y, Hoogland S, Rothenberger A, Katsiev K, Losovyj Y, Zhang X, Dowben P.A, Mohammed O.F, Sargent E.H, and Bakr O.M. “Low trap-state density and long carrier diffusion in organolead trihalide perovskite single crystals”. *Science* **347**, 6221 (2015).



- 
- <sup>27</sup> Ponseca C.S. and Sundstrom V. “Revealing the ultrafast charge carrier dynamics in organo metal halide perovskite solar cell materials using time resolved THz spectroscopy”. *Nanoscale* **8** 6249-6257 (2016).
- <sup>28</sup> Wehrenfennig C, Eperon G. E, Johnston M. B, Snaith H. J, Herz L. M. “High Charge Carrier Mobilities and Lifetimes in Organolead Trihalide Perovskites”. *Adv. Mater.* **26**, 1584-1589 (2014).
- <sup>29</sup> Maynard B, Long Q, Schiff E.A, Yang M, Zhu K, Kottokkaran R, Abbas H, and Dalal V.L. “Electron and hole drift mobility measurements on methylammonium lead iodide perovskite solar cells”. *App. Phys. Lett.* **108**, 173505 (2016).
- <sup>30</sup> Schiff E. A. “Low-mobility solar cells: a device physics primer with application to amorphous silicon”. *Sol. Ener. Mat. & Sol. Cells.* **78** 567-595 (2003).
- <sup>31</sup> Chen W, Liu F-. Z, Feng X-. Y, Djuricic A. B, Chan W. K, and He Z-. B. “Cesium Doped NiO<sub>x</sub> as an Efficient Hole Extraction Layer for Inverted Planar Perovskite Solar Cells”. *Adv. Ener. Mat.* **7** 1700722 (2017).
- <sup>32</sup> Abbas H, Kottokkaran R, Samiee M, Zhang L, Ganapathy B, Kitahara A, Noack M, and Dalal V.L. *Appl. Phys. Lett. Mat.* **3**, 016105 (2015).
- <sup>33</sup> Zhou Y, Yang M, Wu W, Vasiliev A.L, Zhu K, and Pature N.P. *J. Mater. Chem. A*, **3**, 8178 (2015).
- <sup>34</sup> Niu G, Li W, Meng F, Wang L, Dong H, and Qiu Y. Study on the stability of CH<sub>3</sub>NH<sub>3</sub>PbI<sub>3</sub> films and the effect of post-modification by aluminum oxide in all-solid-state hybrid solar cells. *J. Mater. Chem. A* **2**, 705–710 (2014).
- <sup>35</sup> Samiee M, Konduri S, Ganapathy B, Kottokkaran R, Abbas H. A, Kitahara A, Joshi P, Zhang L, Noack M, and Dalal V. *Appl. Phys. Lett.* **105**, 153502 (2014).

- 
- <sup>36</sup> Scher H. and Montroll E. *Phys. Rev. B* **12**, 2455 (1975).
- <sup>37</sup> Wang Q, Anonidis H, Schiff E.A. “Electron-drift-mobility measurements and exponential conduction-band tails in hydrogenated amorphous silicon-germanium alloys”. *Phys. Rev. B.* **47** 15 (1993).
- <sup>38</sup> ben-Avraham D. and Havlin S. Diffusion and Reactions in Fractals and Disordered Systems. Cambridge University Press (2000).
- <sup>39</sup> Karl N. “Charge carrier transport in organic semiconductors”. *Synth. Metals* **133-134** 649-657 (2003).
- <sup>40</sup> Rao P.N, Schiff E.A, Tsybeskov L, and Fauchet P. *Chem. Phys.* **284** 129–138 (2002).
- <sup>41</sup> Pecchia A, Gentilini D, Rossi D, Auf der Maur M, Di Carlo A. “Role of Ferroelectric Nanodomains in the Transport Properties of Perovskite Solar Cells”. *Nano Letts.* **16** 988-992 (2016).
- <sup>42</sup> Maynard B, Long Q, Schiff E.A, Yang M, Zhu K, Kottokkaran R, Abbas H, Dalal V.L. “Electron and hole drift mobility measurements on methylammonium lead iodide perovskite solar cells”. *App. Phys. Lett.* **108**, 173505 (2016).
- <sup>43</sup> Shi D, Adinolfi V, Comin R, Yuan M, Alarousu E, Buin A, Chen Y, Hoogland S, Rothenberger A, Katsiev K, Losovyj Y, Zhang X, Dowben P.A, Mohammed O.F, Sargent E.H, and Bakr O.M. “Low trap-state density and long carrier diffusion in organolead trihalide perovskite single crystals”. *Science* **347**, 6221 (2015).
- <sup>44</sup> Ponseca C.S. and Sundstrom V. “Revealing the ultrafast charge carrier dynamics in organo metal halide perovskite solar cell materials using time resolved THz spectroscopy”. *Nanoscale* **8** 6249-6257 (2016).

- 
- <sup>45</sup> Wehrenfennig C, Eperon G. E, Johnston M. B, Snaith H. J, Herz L. M. “High Charge Carrier Mobilities and Lifetimes in Organolead Trihalide Perovskites”. *Adv. Mater.* **26**, 1584-1589 (2014).
- <sup>46</sup> Chen Y, Yi H.T, Wu X, Haroldson R, Gartstein Y.N, Rodionov Y.I, Tikhonov K.S, Zakhidov A, Zhu X.-Y, and Podzorov V. “Extended carrier lifetimes and diffusion in hybrid perovskites revealed by Hall effect and photoconductivity measurements”. *Nat. Comm.* 7:12253 DOI: 10.1038. (2016).
- <sup>47</sup> Stoumpos C.C, Malliakas C.D, Kanatzidis M.G. “Semiconducting Tin and Lead Iodide Perovskites with Organic Cations: Phase Transitions, High Mobilities, and Near-Infrared Photoluminescent Properties”. *Inorg. Chem.* **52**, 9019-9038 (2013)
- <sup>48</sup> Hall E. H. “On a New Action of the Magnet on Electric Currents”. *Am. J. Math.* **2**, 3 p.287 (1879).
- <sup>49</sup> Mott N. Conduction in Non-Crystalline Materials. Oxford Science Publications, (1987).
- <sup>50</sup> Ashcrot N. W, Mermin D. N. Solid State Physics. W.B. Saunders Company p.15 (1976).
- <sup>51</sup> Wehrenfennig C, Eperon G. E, Johnston M. B, Snaith H. J, Herz L. M. “High Charge Carrier Mobilities and Lifetimes in Organolead Trihalide Perovskites”. *Adv. Mater.* **26**, 1584-1589 (Supplementary Materials) (2014).
- <sup>52</sup> Mott N.F and Gurney R.W. Electronic processes in ionic crystals. Oxford University Press, (1940).
- <sup>53</sup> Shi D, Adinolfi V, Comin R, Yuan M, Alarousu E, Buin A, Chen Y, Hoogland S, Rothenberger A, Katsiev K, Losovyj Y, Zhang X, Dowben P.A, Mohammed O.F, Sargent E.H, and Bakr O.M. “Low trap-state density and long carrier diffusion in organolead trihalide perovskite single crystals”. *Science* **347**, 6221 Supplementary Materials (2015).

- 
- <sup>54</sup> Prasanna R. “Transport in Disordered Silicon Materials” dissertation, Syracuse University (1999).
- <sup>55</sup> Kim, H.-S. *et al.* “Lead iodide perovskite sensitized all-solid-state submicron thin film mesoscopic solar cell with efficiency exceeding 9%”. *Sci. Rep.* **2**, 591 (2012).
- <sup>56</sup> Lee, M. M., Teuscher, J., Miyasaka, T., Murakami, T. N. & Snaith, H. J. Efficient hybrid solar cells based on meso-superstructured organometal halide perovskites. *Science* **338**, 643–647 (2012).
- <sup>57</sup> Stranks, S. D. *et al.* Electron–hole diffusion lengths exceeding 1 micrometer in an organometal trihalide perovskite absorber. *Science* **342**, 341–344 (2013).
- <sup>58</sup> Noh J. H, Im S. H., Heo J. H., Mandal T. N, Seok S. I. Chemical management for colorful, efficient, and stable inorganic-organic hybrid nanostructured solar cells. *Nano Lett.* **13**, 1764–1769 (2013).
- <sup>59</sup> Yang W. S, Noh J. H, Jeon N. J, Kim Y. C, Ryu S, Seo J, Seok S. I. “High-performance photovoltaic perovskite layers fabricated through intramolecular exchange”. *Science* **348** (6240):1234-1237 (2015). [quotes an efficiency of 20.2 using FAPbI<sub>3</sub>]
- <sup>60</sup> NREL Best Research-Cell Efficiencies. Rev April 25<sup>th</sup> (2018).
- <sup>61</sup> Wu Y, Xie F, Chen H, Yang X, Su H, Cai M, Zhou Z, Noda T, Han L. “Thermally Stable MAPbI<sub>3</sub> Perovskite Solar Cells with Efficiency of 19.19% and Area over 1 cm<sup>2</sup> Achieved by Additive Engineering”. *Adv. Mater.* **29**, 1701073, DOI: 10.1002/adma.201701073 (2017).
- <sup>62</sup> Kayes B. M, Nie H, Twist R, Spruytte S.G, Reinhardt F, Kizilyalli I.C, and Higashi G.S. “27.6% Conversion efficiency, a new record for single-junction solar cells under 1 sun illumination”. *37th IEEE Photovoltaic Specialists Conference*, 4–8 (2011).

## VITA

Name of Author : Brian Maynard

Place of Birth : Buffalo, NY, USA

Date of Birth : March 17, 1986

Undergraduate : SUNY Potsdam, Potsdam, NY, USA

School Attended

Degrees Awarded : B. A. Mathematics, SUNY Potsdam 2008  
B. A. Physics, SUNY Potsdam 2008

Professional : Teaching Assistant, Physics, Syracuse University

Experience : Summer Instructor, Astronomy, Syracuse University  
Research Assistant, Physics, Syracuse University  
College Reading and Learning Association Master Level Certified,  
CLASS Office, Syracuse University